fibers

MDPI

Article

A Surface-Energy-Based Extension of the Cox–Krenchel Model for Stiffness Prediction of Short-Fiber-Reinforced Thermoplastics

Matthias Bruchmüller

Plastics Technology Group, Faculty of Mechanical Engineering and Thuringian Center of Innovation in Mobility, Technische Universität Ilmenau, 98693 Ilmenau, Germany; matthias.bruchmueller@tu-ilmenau.de

Highlights

What are the main findings?

- The classical Cox–Krenchel model captured the general stiffness trend of the investigated short-fiber-reinforced thermoplastics, but overestimated the modulus of the PP-based systems while describing the PA–basalt system well.
- Within the investigated dataset, the addition of a surface-energy-based adhesion efficiency factor reduced the remaining prediction error and improved agreement between the calculated and measured Young's moduli without changing the basic analytical structure of the model.

What are the implications of these findings?

- The results indicate that fiber morphology remains the primary basis for stiffness prediction, while interfacial compatibility may provide a useful additional descriptor for residual system-dependent deviations.
- For the investigated materials, the proposed extension appears to be a practical way to refine stiffness prediction using accessible surface-energy data, although broader validation across further material systems is still required.

Abstract

Short-fiber-reinforced thermoplastics are widely used in lightweight structural applications, but reliable prediction of their Young's modulus remains challenging because classical analytical models usually neglect interfacial effects. In this study, the Cox–Krenchel model was extended by an adhesion efficiency factor derived from surface-energy-based interfacial tension to account for incomplete elastic load transfer at the fiber–matrix interface. Injection-molded polypropylene (PP) and polyamide 6.6 (PA 6.6) composites reinforced with basalt and glass fibers were produced and characterized experimentally. Model inputs comprised the matrix and fiber modulus, measured fiber volume fraction, experimentally determined individual fiber lengths incorporated through an effective Cox length efficiency factor, and experimentally determined fiber orientation factors. Interfacial tension was calculated from polar and dispersive surface-tension components using the Owens–Wendt–Rabel–Kaelble approach. The classical Cox–Krenchel model described the PA–basalt system with high accuracy but systematically overestimated the stiffness of the PP-based systems. Using a single globally calibrated proportionality constant of $\omega = 0.8$, the adhesion-extended model reduced the mean absolute percentage error on the full condition-specific dataset of 55 data points from 14.2% to 2.7%. The results indicate that morphology remains the dominant basis of stiffness prediction, while surface-energy-based interfacial compatibility

Check for updates

Academic Editor: Chenggao Li

Received: 19 August 2026
Revised: 10 September 2026
Accepted: 14 September 2026
Published: 16 September 2026

Copyright: © 2026 by the author. Licensee MDPI, Basel, Switzerland. This article is an open access article distributed under the terms and conditions of the Creative Commons Attribution (CC BY) license.

provides a relevant additional descriptor for residual system-dependent error. For the investigated systems, the proposed extension improved predictive accuracy while preserving the analytical simplicity of the Cox–Krenchel framework.

Keywords: short-fiber-reinforced thermoplastics; Cox–Krenchel model; stiffness prediction; interfacial adhesion; surface energy

1. Introduction

Short-fiber-reinforced thermoplastics are widely used in lightweight engineering because they combine low density, cost-efficient processing, and adjustable mechanical properties. Injection-molded compounds based on polypropylene (PP) and polyamides (PA), reinforced with glass, basalt, or natural fibers, are highly relevant for structural and semi-structural applications. Their morphology formation, structure–property relationships, and stiffness prediction have therefore been studied extensively [1–3]. For material selection and component design, reliable prediction of the Young's modulus is essential.

Micromechanical models are commonly used to estimate the stiffness of fiber-reinforced polymers from constituent properties and reinforcement morphology. Besides rule-of-mixtures-based approaches, several alternative micromechanical models have been proposed for the stiffness prediction of short-fiber-reinforced polymers, including Halpin–Tsai-type relations, Mori–Tanaka-based mean-field approaches, and Tandon–Weng formulations. However, these approaches also rely on idealizing assumptions and generally do not account explicitly for interfacial adhesion losses in the form addressed here.

While the rule of mixtures provides a useful upper-bound description for continuous fibers aligned with the loading direction, short-fiber-reinforced thermoplastics deviate substantially from this idealized case because finite fiber length and non-ideal fiber orientation reduce the effective reinforcing contribution. To account for these effects, Cox introduced a shear-lag-based length efficiency concept, and Krenchel added an orientation efficiency factor for non-aligned fibers. The resulting Cox–Krenchel framework has become one of the most widely used analytical approaches for predicting the Young's modulus of short-fiber-reinforced polymers [3–10]. At the same time, recent data-driven approaches underline both the practical importance of stiffness prediction and the remaining limitations of purely analytical models [2].

Previous studies have reported that Cox–Krenchel-type predictions can be competitive with, and in several cases more accurate than, alternative analytical approaches such as Halpin–Tsai or Tsai–Pagano for discontinuous fiber systems [3–9]. Good agreement between prediction and experiment has been reported for a range of composite systems, including flax/polypropylene [3], pineapple leaf fiber/epoxy [4], kenaf/epoxy [5], sugar palm fiber/polystyrene [7], kenaf/polypropylene [8], and glass-fiber-reinforced polypropylene when measured fiber orientation and fiber length are used as model inputs [9]. Nevertheless, noticeable deviations remain common. Depending on the fiber–polymer system, the quality of the morphological input data, and the presence of coupling agents or surface treatments, reported differences between the calculated and measured Young's moduli range from below 10% to about 45% [3,5–8]. For example, deviations of up to approximately 45% have been reported for flax-fiber-reinforced polypropylene [6], and substantial errors were also observed for flax/PP systems without coupling agents [3]. More generally, recent work has emphasized that commonly used analytical models are still insufficiently accurate for practical stiffness prediction in randomly oriented short-fiber composites [11]. Conversely, very good agreement has been obtained for systems with favorable interfacial conditions,

such as glass-fiber-reinforced polypropylene with coupling agents [9] and carbon-fiber-reinforced polyamide 6 [10]. Overall, these findings suggest that commonly used analytical models remain insufficiently accurate for general stiffness prediction in heterogeneous short-fiber systems when only morphology-based inputs are considered [3–11].

These observations indicate that deviations between analytical prediction and experiment cannot always be explained by fiber volume fraction, fiber length, and fiber orientation alone. In this context, interfacial shear strength (IFSS) is frequently used as a mechanical descriptor of fiber–matrix interaction, and a variety of experimental methods have been proposed for its determination, including pull-out, fragmentation, microdroplet, and modified short-beam-shear-based approaches [12]. However, such methods are often experimentally demanding, geometry-dependent, or limited in their applicability to specific fiber types and interface configurations [12]. This suggests that, beyond morphology, the efficiency of stress transfer across the fiber–polymer interface is an additional governing factor. This interpretation is consistent with studies showing that interfacial adhesion can be modified substantially by changes in fiber surface state and surface energy, with corresponding effects on interfacial shear strength and wetting behavior, including basalt-fiber-reinforced systems [13]. However, in the present work, the focus is not on interfacial failure phenomena, but on interface-state effects that may already influence elastic load transfer in the small-strain regime [3,5,8].

The role of the interface in composite mechanics has long been discussed in the context of wetting and adhesion [14–19]. Effective load transfer is generally facilitated by adequate wetting and by the formation of an interface state that allows efficient elastic stress transfer in the solidified composite. Thermodynamic descriptions of adhesion commonly relate material interaction to surface energy or surface tension [20–25]. From the perspective of wetting theory, these interactions are reflected in contact-angle relations and interfacial force balance [17,26,27]. Related sessile-drop-based studies also illustrate how contact angle, surface tension, liquid–solid interfacial tension, and the work of adhesion can be linked within a common thermodynamic framework for comparative interface characterization [28]. In polymer and interface science, such concepts are frequently formulated by separating dispersive and polar contributions to the surface energy [29–33]. On this basis, interfacial tension and compatibility between two phases can be estimated for polymer systems [34–41]. Within the Owens–Wendt–Rabel–Kaelble framework, the total surface energy is decomposed into polar and dispersive components, allowing the interfacial tension between two materials to be derived from measurable quantities [29–31,38]. Although surface-energy-based concepts are well-established in adhesion science and in the characterization of modified polymer interfaces [21,25,29–31,33,37,38,40–42], they are not explicitly included in standard analytical stiffness predictions for short-fiber-reinforced thermoplastics.

The present study addresses this gap by introducing an adhesion efficiency factor into the Cox–Krenchel model. The proposed extension is based on the interfacial tension between the fiber and polymer derived from surface-tension components and is intended to represent incomplete elastic load transfer at the interface while preserving the analytical simplicity of the original model. The approach is evaluated for three injection-molded composite systems based on PP and PA 6.6 matrices combined with basalt and glass fibers, for which the fiber volume fraction, fiber length, and fiber orientation were determined experimentally. In addition, the transferability of the proposed concept is explored using an independent literature case for PA 6 composites reinforced with basalt fibers of different surface states [43], combined with literature surface-tension data for PA 6 [44].

Direct mechanical characterization of the interface, for example, by IFSS-based methods, can provide valuable information on fiber–matrix bonding and has been used to assess fiber-surface modification effects [12,13]. However, such methods generally require

dedicated testing concepts and are not always readily transferable across material systems and processing states. Against this background, the aim of this work is to examine whether a surface-energy-based description of fiber–polymer adhesion can reduce the remaining deviation between Cox–Krenchel predictions and experimental Young's moduli across different thermoplastic–fiber combinations without requiring combination-specific mechanical interface tests. The present study introduces a semi-empirical, analytically simple interface-related efficiency term derived from surface-tension-based interfacial tension and intended as a physically motivated correction.

2. Materials and Methods

2.1. Materials

Two thermoplastic matrices and two mineral fiber types were selected to investigate composite systems with different interfacial characteristics. The matrix polymers were polypropylene (PP, Borealis BC612WG, Borealis, Vienna, Austria) and polyamide 6.6 (PA 6.6, Durethan A 30 S, LANXESS, Cologne, Germany). PP was chosen as a low-polar thermoplastic with comparatively low surface tension and a Poisson ratio of 0.44 [45], whereas PA 6.6 was selected as a more polar engineering thermoplastic with higher stiffness, greater potential for interfacial interactions, and a Poisson ratio of 0.35 [46]. Prior to processing, PA 6.6 was dried in a dry-air dryer according to the manufacturer's recommendations to minimize moisture-related effects.

The reinforcing fibers were basalt fibers (BF) and E-glass fibers (GF). The basalt fibers were supplied by Incotelogy GmbH (Pulheim, Germany) as product BR130.1200.11RAI (BCF 13-1200-KV11 int), an assembled continuous-filament roving with a nominal filament diameter of 13 $\pm$ 0.5 µm and a linear density of 1200 tex. According to the supplier, the basalt fiber carried sizing no. 11, a silane-based sizing intended for unsaturated polyester (UP), vinyl ester (VE), and epoxy (EP) systems. The E-glass fibers were supplied as SE1200, 1200 tex, by Owens Corning (Owens Corning Composite Materials, LLC, Toledo, OH, USA), with a silane-based sizing reported as suitable for epoxy, polyester, vinyl ester, polyurethane, and polyamide matrices. No additional coupling agents were introduced during compounding. However, both commercial fiber types were used in their as-supplied state and therefore carried the manufacturer-applied sizing. Consequently, the relevant interface in the present study is the matrix against the as-supplied sized fiber surface rather than the bare mineral substrate. Differences in stiffness prediction should therefore be interpreted in terms of the resulting matrix–sized-fiber interface. The same commercial basalt fiber product, including the same as-supplied sizing, was used in both the PP–BF and PA–BF systems.

The constituent properties required for micromechanical modeling were obtained from mechanical testing, supplier data, and surface-energy characterization, as described in the following sections. The dataset comprises the density and Young's modulus of the neat polymers and reinforcing fibers investigated in this study, as well as the surface-tension values used for interfacial-tension calculations. The latter are reported together with their respective sources in the relevant data sections.

2.2. Composite Preparation

Short-fiber-reinforced thermoplastic compounds were produced by twin-screw compounding and subsequently processed into standardized tensile specimens by injection molding. The processing route was selected to generate composites with defined fiber contents and controlled variations in fiber morphology, particularly fiber length and orientation, which were later used as input parameters for micromechanical modeling.

2.2.1. Compounding

Compounding was carried out using a co-rotating twin-screw extruder (ZSK 40, Werner & Pfleiderer, Stuttgart, Germany) with a screw diameter of 40 mm and a length-to-diameter ratio of 38. Polymer granules and reinforcing fibers were continuously fed into the extruder and melt-compounded under process conditions adapted to the respective matrix material. For PP-based compounds, the maximum barrel temperature was 230 °C, whereas for the PA 6.6-based compounds, it was 310 °C. The screw speed was varied between 50 and 200 min^{-1} depending on the investigated material system.

The compounding conditions were selected to obtain process-stable fiber-reinforced granules for subsequent injection molding while allowing systematic variation of the resulting fiber morphology. After compounding, the extrudates were cooled and pelletized.

2.2.2. Injection Molding

Standardized tensile specimens of type 1A were produced according to DIN EN ISO 527-2 [47] by injection molding and were used for both mechanical testing and subsequent microstructural characterization. The molded specimens were used for mechanical testing and for subsequent characterization of fiber volume fraction, fiber length, and fiber orientation. The specimen geometry is shown in Figure 1.

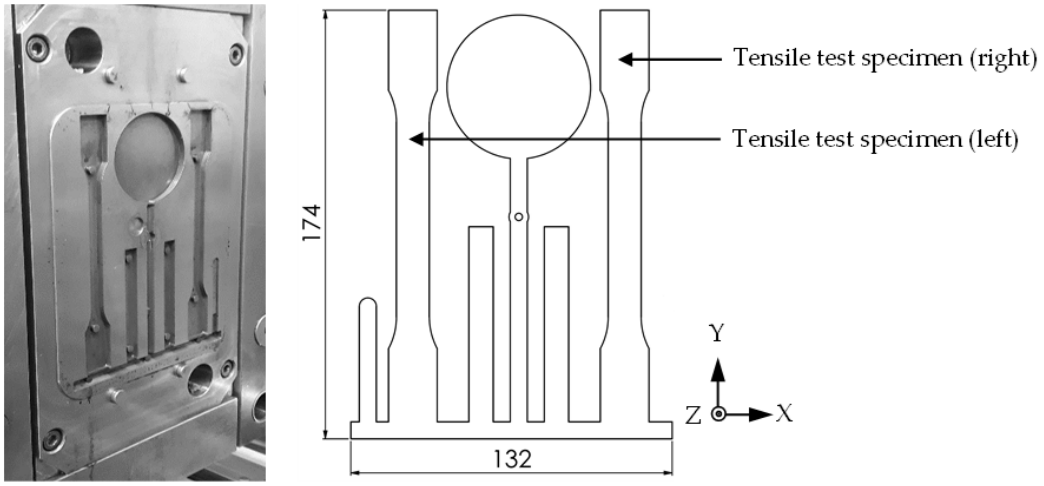

Figure 1. Injection-molded tensile specimen geometry used for mechanical and morphological characterization. Part thickness $t = 4$ mm. Dimension units are in mm.

The injection-molding conditions were adjusted to the respective polymer system and were varied deliberately to influence the fiber morphology in the final specimens. Melt temperature, back pressure, and plasticizing screw speed were modified within defined processing windows. For PP-based compounds, melt temperatures between 220 °C and 260 °C were applied. For PA 6.6-based compounds, the melt temperature was 280 °C. In the case of PA 6.6, a spring-loaded shut-off nozzle was used to ensure stable processing of the dried material. This difference in nozzle configuration is also relevant for subsequent interpretation of the resulting fiber morphology, because it may influence the local flow field and mixing state immediately before cavity entry.

For each material system, several processing conditions were selected to generate specimens with different fiber lengths, and consequently, different stiffness-relevant morphology states. All specimens were produced using the same mold geometry to ensure comparability in the subsequent tensile and microstructural analyses. The full set of investigated processing conditions for all condition IDs is provided in Supplementary Table S1.

2.3. Mechanical Testing

The Young's modulus of the neat polymers and fiber-reinforced composites was determined by tensile testing using type 1A injection-molded specimens according to DIN EN ISO 527-2 [47]. All tests were performed at 23 °C on a universal testing machine (AG-XD 50 kN, Shimadzu, Kyoto, Japan). Strain for modulus determination was measured using an MFA25 extensometer with a gauge length of 50 mm. The crosshead speed used for modulus determination was 1 mm min^{-1}.

For each material condition, at least six specimens were tested. The Young's modulus was evaluated according to DIN EN ISO 527-1 [48] from the extensometer-based strain signal in the prescribed strain interval of 0.05–0.25%. Mean values and the corresponding relative scatter were used for subsequent comparison with the analytical model predictions.

The tensile experiments served two purposes in the present study. First, they provided the reference Young's moduli of the neat matrix polymers required as constituent input data for micromechanical modeling. Second, they yielded the experimental stiffness values of the short-fiber-reinforced composites used to assess the predictive performance of the classical Cox–Krenchel model and of the adhesion-extended formulation proposed in this work.

2.4. Morphological Characterization

The influence of compounding and injection molding on the resulting fiber morphology is well-documented for short-fiber-reinforced thermoplastics [1,3]. The micromechanical models evaluated in this study require experimental input parameters describing the reinforcement morphology in the molded specimens. Therefore, fiber volume fraction, fiber length, fiber orientation, and fiber dispersion were characterized for all investigated composite systems. These parameters were subsequently used as input variables for the Cox–Krenchel model and its adhesion-extended version.

2.4.1. Fiber Volume Fraction

The actual fiber volume fraction of the composites was determined by calcination according to DIN EN ISO 1172 [49]. For this purpose, polymer samples were heated to 480 °C and held for 5 h to thermally remove the polymer matrix, after which the remaining mineral fibers were weighed. Although DIN EN ISO 1172 is primarily formulated for glass-fiber-reinforced materials, the same calcination procedure was applied consistently to all investigated mineral-fiber systems in the present study to ensure comparability. The residual mass was converted into fiber volume fraction using the known densities of the constituent materials. For each processing condition, at least three measurements were performed and averaged.

The experimentally determined fiber volume fractions were used for all model calculations to avoid deviations arising from differences between the nominal and actual fiber contents.

2.4.2. Fiber Length

Fiber length was determined after removal of the polymer matrix by calcination. For this purpose, the composite samples were heated to 480 °C and held for 5 h, after which the separated fibers were recovered for optical analysis. The separated fibers were analyzed by optical microscopy (Stemi 2000-C, Carl Zeiss, Baden-Württemberg, Germany) using digital image acquisition. For each experimental condition, multiple images were evaluated, resulting in at least 2692 measured fibers per material system. High magnifications of the separated fibers enabled the operator to measure all fibers visible in the image, while

additional low-magnification views were used to capture fibers extending beyond the close-up field of view.

In the model evaluation, the measured individual fiber lengths were used to determine the Cox length efficiency factor. For each individually measured fiber length, an individual Cox factor was calculated, and an effective overall length efficiency factor was then obtained for the respective material system by length-weighted averaging, as described in Section 3.1. Mean weight-average fiber lengths and corresponding standard deviations are additionally reported as descriptive morphology parameters but were not used directly in the stiffness calculations. The resulting fiber lengths reflect the morphology after compounding and injection molding and thus represent the effective reinforcement state of the tested specimens. The calcination procedure was applied identically to all compared materials to minimize systematic effects on the extracted fiber-length data.

2.4.3. Fiber Orientation

Fiber orientation was determined from polished sections prepared in orthogonal planes of the injection-molded tensile specimens. Because injection molding produces a characteristic shell–core orientation profile, different regions of the specimen cross-section were evaluated separately. The local fiber angles measured in the section planes were combined to estimate the three-dimensional orientation state, from which the global Krenchel orientation factor was calculated.

Because the orientation factor directly enters the Cox–Krenchel model, the orientation state of the fibers was determined experimentally from polished sections in orthogonal planes. The evaluation procedure is illustrated in Figure 2.

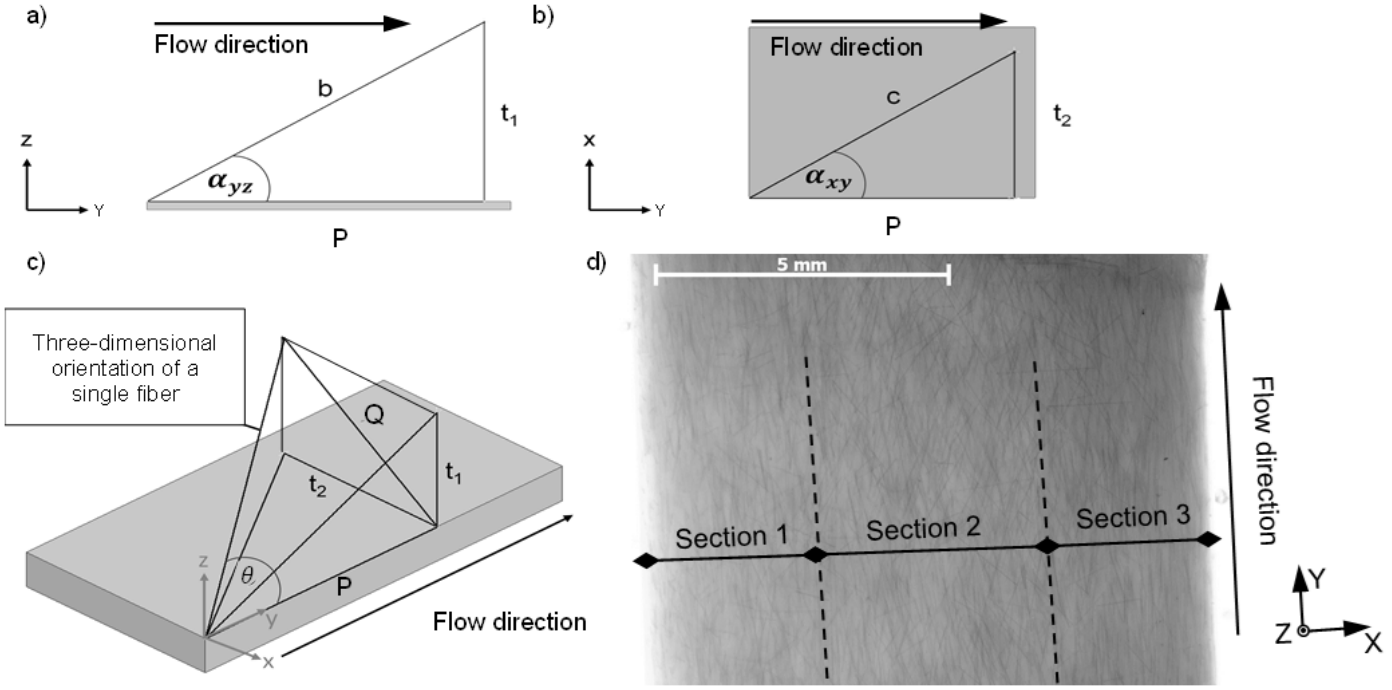

Figure 2. Determination of fiber orientation from polished sections and reconstruction of the three-dimensional orientation angle. The two-dimensional orientation angle was measured in the YZ plane (**a**) and in the XY plane (**b**) and combined to obtain the three-dimensional orientation angle θ (**c**). Measurements were performed in three sections per plane, resulting in nine subsections in total (**d**).

This procedure enabled the local section information to be converted into an effective three-dimensional orientation descriptor for stiffness prediction.

The resulting orientation factor was used directly for Young's modulus prediction within the Cox–Krenchel framework. This procedure allowed the actual orientation state of the molded specimens to be considered instead of assuming an idealized random or fully aligned fiber arrangement. Because the global orientation factor represents an effective average over a spatially heterogeneous orientation field, it reflects not only specimen geometry but also material- and process-specific flow effects, including nozzle-induced changes in melt mixing and fiber kinematics before cavity filling.

2.4.4. Fiber Dispersion

Since the Cox–Krenchel model assumes a homogeneous distribution of reinforcing fibers within the matrix, fiber dispersion was assessed qualitatively by light microscopy on polished cross-sections and by the inspection of fracture surfaces. These analyses were used to identify possible fiber agglomerates or fiber-free regions that could influence the mechanical response independently of fiber length or orientation.

No pronounced agglomeration or fiber-free regions were observed in the investigated materials. The specimens were therefore treated as sufficiently homogeneous for application of the micromechanical modeling approach.

2.5. Surface Energy Characterization

To quantify the interfacial interaction between the fiber and matrix, the surface tension components of the investigated materials were determined and used to calculate the interfacial tension between the respective fiber–polymer combinations. The evaluation followed established concepts of wettability and surface-free-energy analysis based on contact-angle measurements and component-based surface-tension models [17,29–32,38]. The relevance of such surface-energy-based descriptors for fiber–polymer interaction is also supported by interface studies showing that changes in fiber surface energy can modify wetting behavior and interfacial shear strength [13]. The general use of contact-angle-based approaches to relate wettability, surface tension, interfacial tension, and the work of adhesion has also been demonstrated in other material systems, underscoring the broader applicability of such thermodynamic descriptors for comparative interface assessment [28]. The resulting interfacial tension values served as the basis for the adhesion efficiency factor introduced in the extended Cox–Krenchel model.

2.5.1. Determination of Surface Tension Components

The surface tension of the reinforcing fibers was determined by dynamic contact angle measurements using a K100 tensiometer (Krüss, Hamburg, Germany) based on the Wilhelmy method. Measurements were carried out with deionized water and diiodomethane as test liquids. Before analysis, the fibers were cleaned and dried under controlled conditions. For each fiber type, repeated measurements were performed and averaged.

The surface tension of the solid polymer surfaces was determined from contact angle measurements using the sessile-drop method. Polymer plates and films were prepared from the respective neat matrices and measured with the same probe liquids under ambient laboratory conditions. The measured contact angles were used to calculate the dispersive and polar fractions of the surface tension.

For the reinforcing fibers, the dynamic contact-angle measurements characterize the as-supplied fiber surface including the manufacturer-applied sizing. This is the physically relevant surface for wetting and interfacial interaction during composite processing. Accordingly, the reported fiber surface-tension components do not represent bare basalt or bare glass, but the effective commercial fiber surface that was exposed to the polymer matrix in the investigated compounds.

For all investigated materials, the total surface tension and its polar and dispersive components were evaluated using the Owens–Wendt–Rabel–Kaelble method. Where literature data were additionally considered for comparison or validation purposes, the corresponding source is stated explicitly in the Results and Discussion section. The values used in the final model calculations are summarized, together with their sources, in the respective data tables.

2.5.2. Calculation of Interfacial Tension

The interfacial tension between the fiber and polymer was calculated from the surface-tension components according to the Owens–Wendt–Rabel–Kaelble approach. For each fiber–polymer combination, the dispersive and polar contributions of both constituents were combined to determine the corresponding interfacial tension. The use of interfacial tension as a comparative descriptor of material compatibility is consistent with established treatments of polymer interfaces and adhesion thermodynamics [33–35,41].

In the present context, the resulting interfacial tensions therefore refer to the polymer against the as-supplied sized-fiber surface. This is advantageous for practical composite assessment because it captures the real matrix-facing fiber surface of the commercial reinforcement, although substrate and sizing effects cannot be separated in the present study.

In the present study, lower interfacial tension was interpreted as an indicator of more favorable thermodynamic compatibility, and consequently, more effective interfacial load transfer under elastic loading. The calculated interfacial tension values were therefore used as physically motivated descriptors of relative interfacial quality rather than as direct mechanical strength parameters.

2.6. Model Input Parameters and Evaluation Procedure

The prediction of composite stiffness was based on experimentally determined constituent and morphology parameters. The analytical expressions of the classical and adhesion-extended Cox–Krenchel models into which these input parameters were inserted are introduced in Section 3. Sections 3.1–3.4 define the constitutive equations, efficiency factors, interfacial-tension-based adhesion term, and evaluation procedure used for stiffness prediction. For each investigated material system, the Young's modulus of the matrix, the Young's modulus of the reinforcing fiber, the fiber volume fraction, the effective Cox length efficiency factor derived from the individually measured fiber lengths by length-weighted averaging, and the fiber orientation factor were used as input parameters for the classical Cox–Krenchel model. In the adhesion-extended model, the surface-tension components of the fiber and polymer and the resulting interfacial tension were additionally included to calculate the adhesion efficiency factor.

For all composite systems, stiffness predictions were first calculated using the classical Cox–Krenchel framework. In a second step, the proposed adhesion efficiency factor was introduced as an additional multiplicative term to account for incomplete interfacial load transfer. This procedure enabled a direct comparison between the conventional geometric-micromechanical description and the surface-energy-based model extension while keeping all other input conditions identical.

The predicted Young's moduli were compared with the experimentally measured values obtained from tensile testing. Model performance was evaluated based on absolute and relative prediction errors between the predicted and measured stiffness values. Where appropriate, averaged error measures were additionally used to assess the overall predictive quality of the classical and extended model variants across the full condition-specific dataset. In addition, a grouped leave-one-material-system-out cross-validation was performed on the condition-specific dataset as a robustness check.

All input parameters used for model evaluation are summarized in the corresponding tables. In addition, the complete condition-specific experimental and model-evaluation values are provided in Supplementary Table S2. This includes the measured Young's modulus, measured fiber volume fraction, weight-average mean fiber length, effective Cox length efficiency factor, orientation factor, and the corresponding classical and adhesion-extended model predictions.

3. Theoretical Background and Model Development

3.1. Classical Cox–Krenchel Model

The Young's modulus of short-fiber-reinforced thermoplastics was first described using the classical Cox–Krenchel approach. In this framework, the composite modulus is expressed as a function of the matrix modulus, the fiber modulus, the fiber volume fraction, and efficiency factors accounting for fiber orientation and fiber length. The model assumes that the reinforcing fibers contribute to composite stiffness according to their intrinsic stiffness and their effective load-bearing capability within the matrix. Accordingly, the composite modulus E_c can be written as Equation (1), in which the fiber contribution is reduced by orientation and length efficiency factors.

$$E_c = E_m\left(1 - V_f\right) + \eta_o \overline{\eta_l} E_f V_f, \tag{1}$$

where E_m is the Young's modulus of the matrix, E_f is the Young's modulus of the fiber, V_f is the fiber volume fraction, η_o is the orientation efficiency factor, and $\overline{\eta_l}$ is the effective Cox length efficiency factor obtained from the individually measured fiber lengths of the respective material system by length-weighted averaging.

To account for the reduced reinforcing efficiency of discontinuous fibers, Cox introduced the length efficiency factor given in Equation (2):

$$\eta_l = 1 - \frac{\tanh\left(\beta \frac{l_i}{2}\right)}{\beta \frac{l_i}{2}} \tag{2}$$

where l_i is the length of an individual measured fiber and β is the shear-lag parameter. The shear-lag parameter β is calculated according to Equation (3):

$$\beta = \sqrt{\frac{2\pi\, G_m}{E_f\, A_f \ln\left(\frac{R}{r}\right)}} \tag{3}$$

where G_m is the shear modulus of the matrix, A_f is the fiber cross-sectional area, R is the mean distance between neighboring fibers, and r is the fiber radius.

The mean distance between fibers was estimated from the fiber volume fraction under the assumption of a homogeneous fiber distribution within the composite. For this purpose, a hexagonal packing arrangement was assumed in the cross-sectional plane, yielding:

$$R = \sqrt{\frac{2 \cdot \pi \cdot r^2}{\sqrt{3} \cdot V_f}} \tag{4}$$

Based on Equations (2)–(4), an individual length efficiency factor $\eta_l(l_i)$ was calculated for each experimentally measured fiber length. To account for the measured fiber population directly, an effective global length efficiency factor $\overline{\eta_l}$ was then obtained by length-weighted averaging of the individual values:

$$\overline{\eta_l} = \frac{\sum \eta_l(l_i) \cdot l_i}{\sum l_i} \quad (5)$$

where l_i is the length of the i-th measured fiber and $\eta_l(l_i)$ is the corresponding individual Cox length efficiency factor.

The orientation efficiency factor η_o was determined according to Equation (6):

$$\eta_o = \sum a_i \, cos^4\theta_i \quad (6)$$

where a_i denotes the fraction of fibers belonging to orientation sector i, and θ_i is the corresponding three-dimensional fiber orientation angle relative to the loading direction.

The orientation factor η_o accounts for deviations from ideal unidirectional fiber alignment and was determined experimentally from the measured fiber orientation state of the injection-molded specimens. The individual length efficiency factor $\eta_l(l_i)$ describes the reduced reinforcing effect of a discontinuous fiber of length l_i. For model evaluation, the experimentally measured fiber population was represented by the effective global factor $\overline{\eta_l}$, obtained by length-weighted averaging of the individual Cox factors calculated for the measured fiber lengths. Although this model has been widely applied to short-fiber composites, it does not explicitly account for differences in fiber–matrix adhesion. In its conventional form, interfacial load transfer is only considered implicitly through the geometric efficiency terms. In different forms, this model framework has been widely used for stiffness estimation in discontinuous fiber composites [3–5,7–9,11,43]. The experimentally determined orientation and length descriptors were inserted into Equations (2)–(6) and subsequently used in the stiffness prediction according to Equation (1).

3.2. Adhesion-Based Extension of the Cox–Krenchel Model

To account for differences in interfacial compatibility between the investigated fiber–polymer systems, the classical Cox–Krenchel model was extended by introducing an additional adhesion efficiency factor, η_a.

In the present context, the term adhesion is not used in a fracture-mechanical sense of interfacial debonding, sliding, or pull-out, which are more directly related to composite strength and failure. Instead, the proposed interface-related factor is intended to represent differences in the efficiency of elastic stress transfer in the small-strain regime while the interface is still macroscopically intact. Such differences may arise, for example, from incomplete molecular-scale contact established during wetting and solidification, interfacial microvoids or poorly wetted regions, a compliant interphase of altered local structure, or relaxation effects associated with residual thermal stresses. Any of these effects can reduce the effective stiffness contribution of the fibers without requiring visible interfacial failure. Within this interpretation, surface-energy-based interfacial compatibility is not treated as a direct mechanical strength parameter, but as a physically motivated descriptor of interface states that may influence the elastic load-transfer efficiency.

The conceptual basis for such an interface-related efficiency term can be linked to established adhesion theories emphasizing the role of intermolecular interactions, wetting, and interfacial energetics in load transfer across bonded material combinations [21–25,32,33,41]. The physical motivation for the additional adhesion efficiency factor is illustrated schematically in Figure 3.

The schematic emphasizes that non-ideal interfacial compatibility does not change the intrinsic fiber stiffness but reduces the effectively transferable elastic contribution. This reduction is conceived here as an interphase- or contact-quality effect in the intact elastic regime, not because of fully developed interfacial failure. The introduction of η_a does not replace the geometric efficiency factors but complements them by incorporating an

interface-related contribution. In this way, fiber orientation, fiber length, and interfacial compatibility are treated as distinct but interacting influences on stiffness development.

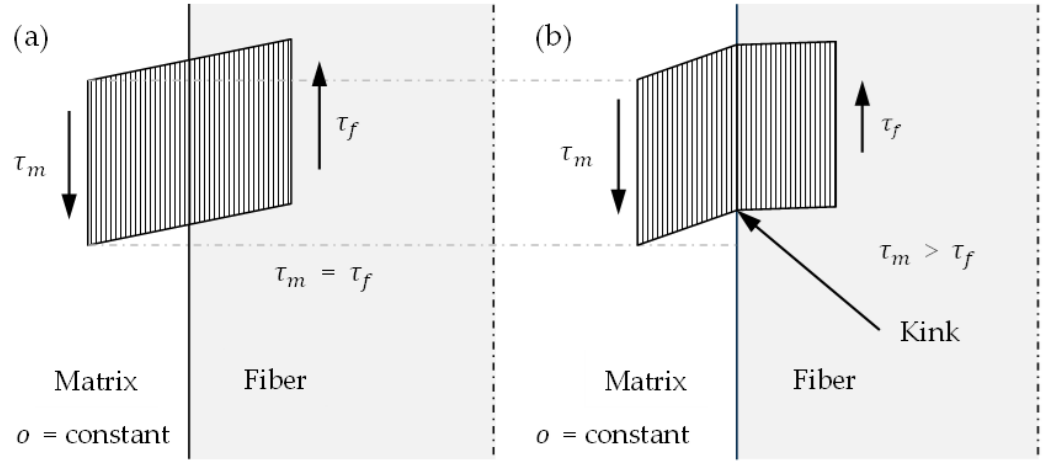

Figure 3. Schematic illustration of ideal (**a**) and reduced (**b**) elastic load transfer at the fiber–matrix interface. Under ideal interfacial conditions, the load is transferred without losses across the interface, whereas non-ideal interfacial compatibility reduces the effective stress transfer from the matrix to the fiber and thereby lowers the reinforcing contribution to the composite stiffness.

3.3. Calculation of the Adhesion Efficiency Factor

In the present study, the adhesion efficiency factor was related to the thermodynamic compatibility of the fiber and matrix as described by their interfacial tension γ_{12}.

$$\gamma_{12} = \left(\sqrt{\gamma_1^d} - \sqrt{\gamma_2^d}\right)^2 + \left(\sqrt{\gamma_1^p} - \sqrt{\gamma_2^p}\right)^2, \tag{7}$$

Interfacial tension was chosen as the descriptor because it combines the polar γ^p and dispersive surface-tension γ^d contributions of both constituents into a single physically interpretable measure of compatibility. Lower interfacial tension was interpreted as indicating more favorable interaction between the fiber and matrix, and consequently, a higher efficiency of elastic load transfer.

To obtain the functional form of the adhesion efficiency factor, an incremental attenuation assumption was adopted. Specifically, it was assumed that an incremental increase in normalized interfacial incompatibility reduces a constant fraction of the remaining transferable elastic fiber contribution. This assumption can be written as:

$$\frac{dE}{E} = -\omega\, d\left(\frac{\gamma_{12}}{\gamma_2}\right) \tag{8}$$

where E denotes the remaining effective elastic contribution of the fiber phase under non-ideal interfacial conditions, γ_{12} is the interfacial tension between the fiber and matrix, γ_2 is the total surface tension of the polymer phase, and ω is a proportionality constant. Integration of Equation (8) from the idealized reference state ($E = E_0$ at $\gamma_{12} = 0$) to the actual state (E at γ_{12}) gives Equation (9):

$$ln\left(\frac{E}{E_0}\right) = -\omega\,\frac{\gamma_{12}}{\gamma_2} \tag{9}$$

and therefore

$$\eta_a = \frac{E}{E_0} = e^{-\omega\,\frac{\gamma_{12}}{\gamma_2}} \tag{10}$$

An alternative first-order assumption would lead to the linear relation given in Equation (11):

$$\eta_a = 1 - \omega \, \frac{\gamma_{12}}{\gamma_2}. \tag{11}$$

Over the comparatively narrow range of normalized interfacial-tension values covered by the present dataset, the linear and exponential forms differed only modestly. The exponential form was retained because it ensures positive efficiency factors, provides a compact attenuation law, and is consistent with the above incremental interpretation. The present dataset, however, does not yet allow for strong discrimination between these alternative functional forms.

Normalization by the polymer surface tension γ_2 was introduced because within the present micromechanical interpretation, the matrix phase is the phase from which load is transferred into the reinforcement. The normalization therefore provides a matrix-referenced dimensionless compatibility measure that remains comparable across the investigated polymer systems. This choice is physically motivated but not unique; alternative normalizations based on other interfacial energy measures may also be considered in future work. In this interpretation, the attenuation law does not imply interfacial failure in the modulus-determination regime. Rather, it represents an effective reduction in elastic stress-transfer efficiency associated with interfacial contact quality and interphase-related effects.

By introducing the adhesion efficiency factor from Equation (10) into the classical Cox–Krenchel framework of Equation (1), the extended stiffness model becomes Equation (12):

$$E_c = E_m \left(1 - V_f\right) + \eta_o \, \overline{\eta_l} \, \eta_a \, E_f \, V_f \tag{12}$$

This formulation retains the established contributions of fiber volume fraction, fiber length, and fiber orientation while additionally accounting for reduced elastic load transfer due to incomplete physical adhesion at the fiber–matrix interface. Interfacial tension is thus used as a comparative descriptor of relative interfacial quality within a unified modeling framework.

Equation (10) shows the expected limiting behavior of the proposed adhesion efficiency factor. For an idealized interface with $\gamma_{12} = 0$, $\eta_a = 1$, so that the classical Cox–Krenchel model is recovered. With increasing interfacial tension, η_a decreases monotonically and correspondingly reduces the transferable fiber-related stiffness contribution. In the limiting case $\eta_a \to 0$, Equation (12) approaches $E_c = E_m\left(1 - V_f\right)$, meaning that the fiber phase no longer contributes effectively to elastic reinforcement. This limiting case should be interpreted as a mathematical boundary of the model rather than as a literal physical description of real composites.

3.4. Evaluation of Model Accuracy

The predictive performance of the classical formulation given by Equation (1) and of the adhesion-extended formulation given by Equation (12) was assessed by comparison with the experimental tensile-test results. For each investigated material system, the same constituent and morphology inputs were used in both model variants, while the adhesion efficiency factor was included only in the extended formulation. This procedure enabled the isolated effect of the interface-related model extension to be evaluated without changing the geometric basis of the Cox–Krenchel description. Model performance was assessed using absolute and relative prediction errors between the predicted and measured Young's modulus values. In addition, averaged error measures across all condition-specific data points were used where appropriate to compare the overall predictive quality of the two model formulations. The comparison was intended to determine whether the inclusion of interfacial tension as an additional descriptor improves stiffness prediction for short-fiber-

reinforced thermoplastics with different fiber–matrix combinations. Both model variants were evaluated using identical constituent and morphology inputs.

4. Results

4.1. Mechanical Properties of Neat Polymers and Composites

Tensile testing according to DIN EN ISO 527-1 [48] and DIN EN ISO 527-2 [47] provided the experimental Young's moduli used for subsequent model evaluation. The moduli of the neat polymers served as matrix input parameters for the analytical calculations, whereas the composite moduli were used as reference values for validating the classical and adhesion-extended Cox–Krenchel models. The experimentally determined matrix properties, together with the fiber properties used in the analytical calculations, are compiled in Table 1.

Table 1. Mechanical properties of the neat polymers and reinforcing fibers used as constituent input parameters for the stiffness prediction.

Material	Density [g cm^{-3}]	Tensile Strength [MPa]	Young's Modulus [MPa]
PP (Borealis BC612WG)	0.90	24.0	1093
PA 6.6 (Durethan A 30 S, dry)	1.14	81.0	3782
Basalt fiber	2.67	3200	80,000
E-glass fiber	2.63	1803	72,200

The neat polymers showed markedly different stiffness levels. Polypropylene (PP, Borealis BC612WG) exhibited a Young's modulus of 1093 MPa, while polyamide 6.6 (PA 6.6, Durethan A 30 S) reached 3782 MPa in the dry-conditioned state [44]. Thus, PA 6.6 was approximately 3.5 times stiffer than PP. The reinforcing fibers showed substantially higher stiffness than both matrices. Basalt fibers exhibited a Young's modulus of 80.0 GPa [50] and E-glass fibers 72.2 GPa [51], confirming their suitability as effective reinforcement phases for stiffness enhancement.

Table 2 summarizes the descriptive system-level mean Young's moduli and the number of condition-specific mean values for each material system. The underlying condition-specific values are reported in Supplementary Table S2. The reported system-level mean values are included for descriptive purposes only and were not used as the primary basis for model calibration or global error evaluation.

Table 2. Descriptive system-level mean Young's moduli and number of condition-specific mean values for the investigated material systems.

Material System	Number of Condition Specific Means	Target Fiber Volume Fraction [vol.%]	Mean Young's Modulus [MPa]	Standard Deviation [MPa]
PP–BF	11	2.5	2130	128
PP–BF	22	7.5	3598	118
PP–GF	16	8.5	3493	38
PA–BF	6	7.5	4862	99

As shown in Table 2, all investigated composites exhibited a clear stiffness increase relative to the respective neat polymer. For PP–BF at a target fiber volume fraction of 2.5%, the condition-specific mean modulus values ranged from 1927 to 2329 MPa. At a target fiber volume fraction of 7.5%, the corresponding range was 3370–3724 MPa. The PP–GF composites at 8.5 vol.% fiber content exhibited mean modulus values between 3454 and

3546 MPa. The highest stiffness values were obtained for PA–BF at 7.5 vol.% fiber content, with condition-specific mean values between 4760 and 4948 MPa.

The experimental scatter remained low for all investigated systems. The coefficient of variation ranged from 2.48% to 3.30% for PP–BF at 2.5 vol.%, from 1.23% to 1.28% for PP–BF at 7.5 vol.%, from 0.30% to 0.40% for PP–GF, and from 1.00% to 1.10% for PA–BF. This good reproducibility is important for the subsequent model assessment, as it allows deviations between the prediction and experiment to be attributed primarily to model limitations rather than to experimental uncertainty.

Overall, the measured stiffness values confirm the expected reinforcing effect of short fibers and reveal clear differences between the investigated material systems. These results provide the experimental basis for the following analysis of morphology-dependent reinforcement effects and for an evaluation of the proposed surface-energy-based model extension.

4.2. Fiber Morphology After Processing

Since the predictive capability of the Cox–Krenchel model depends strongly on the actual reinforcement morphology, the fiber volume fraction, fiber length, and fiber orientation were determined for the investigated composite systems after processing. These parameters were subsequently used as direct input variables for the stiffness calculations.

4.2.1. Fiber Volume Fraction

The fiber volume fractions determined by calcination partly deviated from the nominal target values and were therefore used in the model calculations instead of nominal contents. In particular, the PP–BF systems showed noticeable deviations from their nominal target values, whereas PP–GF and PA–BF were much closer to the intended reinforcement level (Table 3).

Table 3. Experimentally determined fiber volume fractions of the investigated composite systems after processing.

Material System	Target Fiber Volume Fraction [vol.%]	Mean Fiber Volume Fraction [vol.%]	Standard Deviation [vol.%]
PP–BF	2.5	2.356	0.334
PP–BF	7.5	7.260	0.572
PP–GF	8.5	8.511	0.085
PA–BF	7.5	7.644	0.033

Note: The reported standard deviations describe the scatter of repeated measurements for the respective material system.

For the PP–GF composites, the measured fiber volume fraction was 8.511 $\pm$ 0.09 vol.% based on 16 measurements and thus in very close agreement with the nominal value of 8.5 vol.%. Likewise, the PA–BF composites showed an average fiber volume fraction of 7.644 $\pm$ 0.03 vol.% based on 12 measurements, which was also close to the target value of 7.5 vol.%.

These results demonstrate that the actual reinforcement contents were sufficiently reproducible for model validation. At the same time, the deviations between nominal and measured fiber volume fraction confirm that experimentally determined values should be used in the analytical calculations rather than nominal target values.

4.2.2. Fiber Length

The fiber-length results obtained after compounding and injection molding are summarized in Table 4. Since the model evaluation was based directly on the experimentally

measured individual fiber lengths rather than on a single representative fiber length, Table 4 reports the mean weight-average fiber length as a descriptive morphology parameter together with the corresponding effective Cox length efficiency factor $\overline{\eta_l}$ calculated from the measured fiber population by length-weighted averaging. As shown, the PP–BF composites retained the largest residual fiber lengths, whereas the shortest values were found for PA–BF. The reported weight-average fiber lengths serve only as descriptive morphology parameters, whereas the stiffness calculations were based on the effective length efficiency factor $\overline{\eta_l}$ derived from the individual measured fiber lengths by length-weighted averaging.

Table 4. Fiber-length characterization and effective Cox length efficiency factors derived from the individually measured fiber lengths of the investigated composite systems after processing.

Material System	Target Fiber Volume Fraction [vol.%]	Number of Investigated Fibers	Mean Weight Average Fiber Length [µm]	Standard Deviation [µm]	Effective Cox Length Efficiency Factor, $\overline{\eta_l}$ [-]
PP–BF	2.5	6899	1034	142	0.7780
PP–BF	7.5	5710	916	84	0.7229
PP–GF	8.5	2692	933	94	0.7307
PA–BF	7.5	1862	413	40	0.7212

The longest weight-average fiber length was observed for PP–BF at 2.5 vol.%, with 1034 ± 142 µm, whereas the shortest value was measured for PA–BF at 7.5 vol.%, with 413 ± 40 µm. Despite these pronounced differences in residual fiber length, the resulting effective Cox factors lay within a comparatively narrow range. This reflects the fact that the Cox length efficiency factor is not determined by fiber length alone but also depends on the shear-lag parameter β and thus on constituent and geometric model parameters.

The comparison of the two PP–BF compounds suggests that higher fiber content is associated with reduced residual fiber length, which can plausibly be attributed to intensified fiber–fiber interactions and increased fiber breakage during melt processing. Such a reduction in residual fiber length with increasing fiber content is consistent with earlier observations for compounded and injection-molded short-fiber thermoplastics [1,3]. Since fiber length directly affects the load transfer efficiency in short-fiber composites, these differences are expected to contribute to the observed variation in composite stiffness.

4.2.3. Fiber Orientation

The fiber orientation factors were determined from at least 70 fibers per subsection and revealed clear differences between the investigated material systems (Table 5).

Table 5. Experimentally determined fiber orientation factors and corresponding global orientation angles, used for stiffness prediction.

Material System	Fiber Orientation Factor η_o [-]	Propagated SD [-]	Global 3D-Orientation Angle θ [°]	SD [°]
PP–BF 2.5%	0.8728	0.0134	14.853	0.82
PP–BF 7.5%	0.7924	0.0385	19.351	1.93
PP–GF	0.6730	0.0522	25.107	2.32
PA–BF	0.3126	0.0575	41.602	3.10

Note: The orientation factor η_o was derived from the microscopic analysis of polished cross-sections and used as a direct input parameter in the Cox–Krenchel model.

PP–BF at 2.5 vol.% exhibited the highest orientation factor, whereas PA–BF showed the least favorable orientation state with respect to tensile loading. This difference is not attributed to mold geometry, which was identical for all materials, but to process-specific

flow conditions during injection molding. In the PA–BF system, a spring-loaded shut-off nozzle was used. This nozzle configuration likely promoted stronger melt mixing and a more disturbed flow state immediately before entry into the mold cavity, thereby reducing the preferred alignment of fibers in the loading direction. At the same time, the altered flow history was associated with substantially shorter residual fiber lengths. The comparatively low global orientation factor of PA–BF should therefore be interpreted as a process- and morphology-related outcome rather than as an anomalous measurement. Such differences are highly relevant for stiffness prediction because the orientation factor directly scales the effective reinforcing contribution of the fibers within the Cox–Krenchel approach.

4.2.4. Fiber Dispersion

Microscopic inspection did not reveal pronounced fiber agglomeration or fiber-free regions in the investigated compounds. The fiber distribution was therefore considered sufficiently homogeneous for application of the analytical model. This observation is relevant because significant dispersion defects could reduce the measured stiffness independently of fiber length, orientation, or interfacial adhesion.

Overall, the morphological characterization shows that the investigated composite systems differed not only in constituent properties, but also in their effective reinforcement state after processing. Fiber volume fraction, fiber length, and fiber orientation all varied systematically between the materials and therefore had to be considered explicitly in the subsequent stiffness prediction. At the same time, the absence of major dispersion defects supports the interpretation that remaining deviations between the calculated and experimental Young's moduli are mainly related to model limitations, including the description of interfacial load transfer.

4.3. Surface-Tension Components and Interfacial Tension

To assess the thermodynamic compatibility between the matrix and fiber, the polar and dispersive components of surface tension were determined at 23 °C for all investigated constituents and subsequently used to calculate the interfacial tension according to the Owens–Wendt approach. Exact numerical values of the measured surface-tension components are provided in Table 6, while the comparative trends are illustrated in Figure 4.

As shown in Table 6, PA 6.6 exhibited substantially higher polar and dispersive contributions than PP, while both mineral fibers showed pronounced polar surface character. These differences indicate marked variation in the interaction potential of the investigated constituents.

These results provide the basis for the subsequent calculation of interfacial tension.

Based on the measured surface-tension components, the corresponding interfacial tension values were calculated using Equation (7). The resulting values are listed in Table 7 and compared graphically in Figure 5.

Table 6. Polar and dispersive surface-tension components of the investigated matrices and fibers at 23 °C.

Material	Polar Component γ^p [mN m^{-1}]	SD [mN m^{-1}]	Dispersive Component γ^d [mN m^{-1}]	SD [mN m^{-1}]	Total Surface Tension γ [mN m^{-1}]
PA 6.6	10.187	1.650	29.762	0.820	39.949
PP	5.593	0.780	16.680	0.060	22.273
Basalt fiber	25.400	3.100	14.618	0.270	40.018
Glass fiber	24.282	1.720	21.062	0.500	45.344

Table 7. Interfacial tension values calculated according to the Owens–Wendt and Wu approach for the investigated matrix–fiber combinations.

Material System	OWRK-Interfacial Tension γ_{12} [mN m^{-1}]	SD [mN m^{-1}]	WU-Interfacial Tension γ_{12} [mN m^{-1}]	SD [mN m^{-1}]
PP–BF	7.223	1.87	12.80	3.01
PP–GF	6.823	1.23	12.20	1.94
PA–BF	6.080	1.51	11.60	2.74

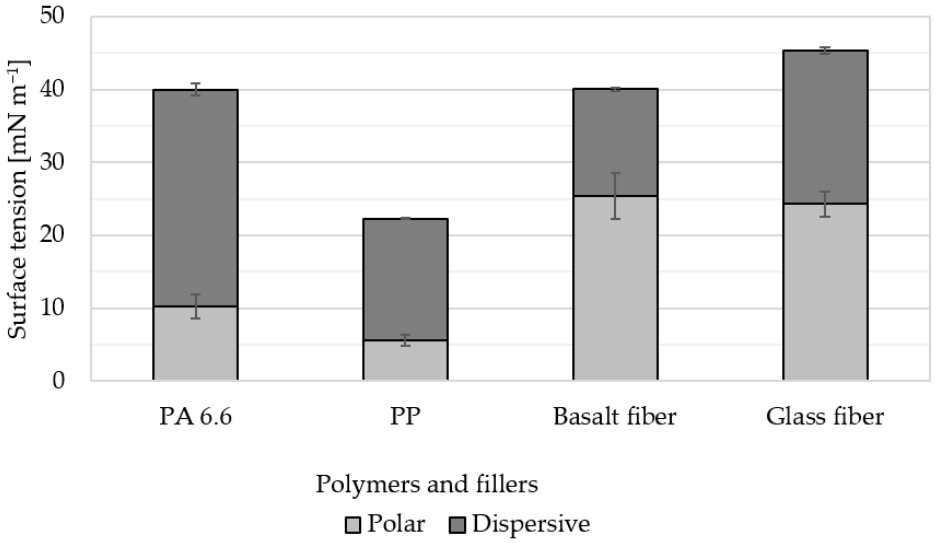

Figure 4. Polar and dispersive surface-tension components of the investigated matrices and reinforcing fibers at 23 °C.

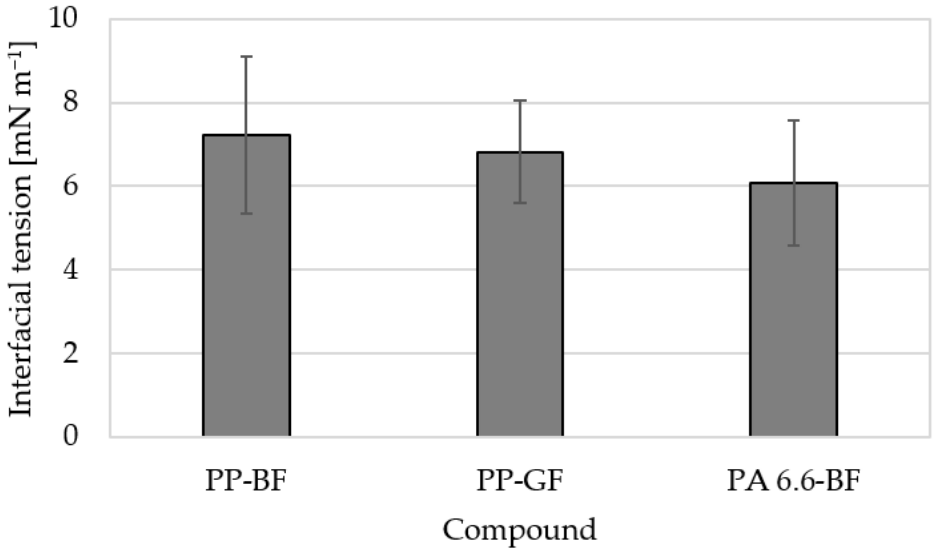

Figure 5. Calculated interfacial tension of the investigated fiber–polymer combinations based on surface-tension components according to the OWRK-interfacial tension.

As shown in Table 7, the PP-based systems exhibited higher interfacial tension than the PA-based system. Among the investigated combinations, PP–BF showed the highest interfacial tension, whereas PA–BF showed the lowest value. Because both approaches yielded the same ranking of material systems, and because the OWRK-based values showed lower standard deviations, the following analysis focused on the OWRK parameter set.

Additionally, the OWRK combining rule was retained as the primary basis of the present analysis because the surface characterization of all constituents was consistently performed within the Owens–Wendt–Rabel–Kaelble framework, in which the total surface tension is decomposed into dispersive and polar components and interfacial tension is derived from the same component set. Using the OWRK relation for both component determination and interfacial-tension calculation therefore provides a methodologically consistent description. The harmonic-mean rule according to Wu was evaluated additionally as a robustness check.

Figure 5 shows the calculated OWRK-interfacial tension γ_{12} for the three fiber–polymer combinations. On average, the PP-based systems lay at higher γ_{12} than the PA-based system, which would be consistent with less favorable wettability and potentially reduced elastic load transfer. However, the observed differences were small relative to their propagated uncertainty. The γ_{12} values should therefore not be interpreted as sharply separated deterministic quantities, but rather as trend-level descriptors of relative interfacial compatibility within the present dataset.

Despite this limited statistical separation, the surface-energy-based descriptor remains a physically motivated, independently measurable quantity that supplements the classical morphology parameters. It therefore provides the rationale for introducing an adhesion efficiency factor η_a into the Cox–Krenchel framework, as developed in the following sections.

4.4. Prediction of Young's Modulus by the Classical Cox–Krenchel Model

The Young's modulus of the investigated short-fiber-reinforced composites was first predicted using the classical Cox–Krenchel model. A key methodological aspect of the present study is that all morphology-dependent model inputs were determined experimentally from the processed specimens rather than being assumed from nominal or idealized values. The model combines the rule of mixtures with efficiency factors that account for finite fiber length and non-ideal fiber orientation in the composite. Accordingly, the predictions were based on experimentally determined material and morphology data, including matrix modulus, fiber modulus, fiber volume fraction, experimentally determined individual fiber lengths incorporated through the effective length efficiency factor $\overline{\eta_l}$, and orientation factor, so that the calculated values reflect the actual microstructural characteristics of the investigated injection-molded composites. This pattern is consistent with previous reports showing that Cox–Krenchel-type approaches can provide good agreement for some systems but substantial overestimation for others, depending on morphology and interface quality [3,6,8,9,11,43]. The Young's moduli shown in Figure 6 were predicted using the classical Cox–Krenchel formulation given by Equation (1), together with the experimentally determined efficiency factors from Equations (2)–(6).

As shown in Figure 6, the classical Cox–Krenchel model reproduced the stiffness of the PA-based composite with high accuracy but showed noticeable deviations for the PP-based systems. For the PA–BF material, the experimentally measured Young's modulus amounted to 4.86 GPa on average, whereas the model predicted a mean value of 4.87 GPa. This corresponded to a slight overestimation of only about 0.1%, indicating that the classical model was well-suited to describe the reinforcing effect in this material system.

A different trend was observed for the PP-based compounds. For PP–BF at a fiber content of 7.5 vol.%, the measured modulus averaged 3.60 GPa, while the Cox–Krenchel model predicted 4.35 GPa. The resulting overestimation of approximately 20.8% indicates that the classical formulation considerably overpredicted the effective reinforcement contribution in this case. A similarly pronounced deviation was obtained for PP–GF, for which the measured mean modulus was 3.49 GPa and the predicted mean modulus was 4.22 GPa, corresponding to an overestimation of about 20.9%.

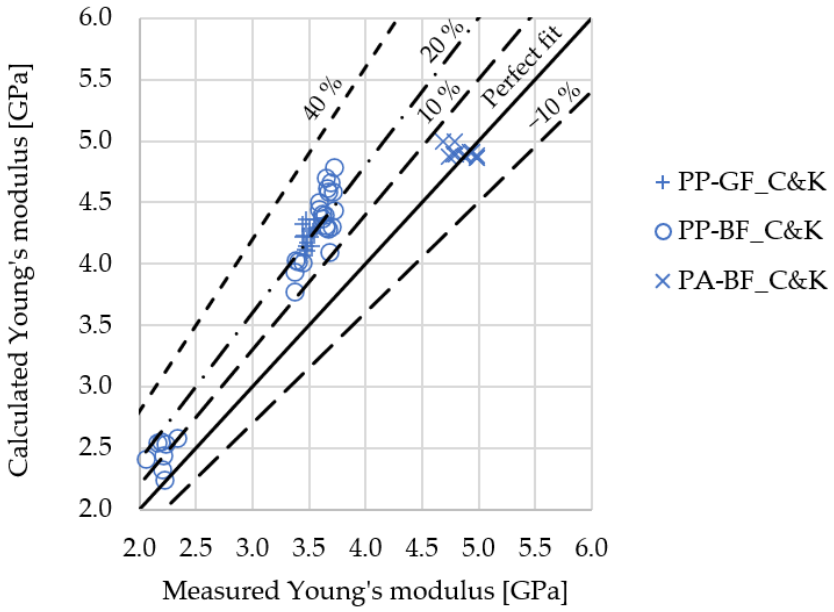

Figure 6. Comparison of the measured and classically predicted Young's moduli using the Cox–Krenchel model (C&K).

For PP–BF at the lower fiber content of 2.5 vol.%, the agreement between the experiment and model was better, although the predicted stiffness remained above the measured value. Here, the experimental modulus averaged 2.13 GPa, whereas the model yielded 2.38 GPa, corresponding to an overestimation of approximately 11.7%. This suggests that the prediction deviation of the classical model became more pronounced with increasing reinforcement content in the PP-based systems.

These results indicate that the classical Cox–Krenchel model captured the fundamental reinforcing effect of short fibers but did not describe all stiffness-relevant mechanisms equally well for all matrix–fiber combinations. Since the model explicitly considers fiber content, fiber stiffness, fiber length, and fiber orientation, the remaining discrepancies must be attributed to factors beyond purely geometric and morphological reinforcement. In particular, the model assumes ideal stress transfer between the matrix and fiber and therefore does not explicitly account for differences in interfacial adhesion.

This interpretation is consistent with the surface-tension analysis presented in the previous section. The PP-based systems showed higher interfacial tensions than the PA-based systems, indicating less favorable thermodynamic compatibility between the matrix and reinforcement. Under such conditions, the actual load transfer from the matrix to fiber may be less efficient than assumed by the classical Cox–Krenchel model, leading to an overestimation of composite stiffness. In contrast, the comparatively low interfacial tension of the PA–BF system agrees with the good predictive accuracy obtained for this material combination.

Overall, the classical Cox–Krenchel model can be regarded as a suitable first-order approximation for predicting the Young's modulus of short-fiber-reinforced thermoplastics. However, the systematic overestimation observed for the PP-based systems shows that morphology-related parameters alone are not sufficient to fully describe the effective reinforcement. This provides the rationale for introducing an additional adhesion-related correction term in the following section to improve modulus prediction across different matrix–fiber combinations.

4.5. Sensitivity Analysis of the Classical and Adhesion-Extended Model

A sensitivity analysis was performed primarily for the classical Cox–Krenchel model to assess whether the remaining deviations between the experiment and model could be explained solely by uncertainty in the input parameters. For the adhesion-extended model, the role of the additional interface-related term was assessed separately in terms of its effect on the predicted modulus.

As a representative case, a PP–BF composite condition from the 7.5% content dataset (condition: PP–BF–7.5–2) was selected, for which the experimentally measured Young's modulus was 3663 MPa and the corresponding classical Cox–Krenchel prediction was 4587 MPa. Each input parameter was then varied individually by ±5% around its reference value while all other parameters were kept constant. The resulting change in predicted Young's modulus was used to compare the relative influence of the different inputs. This approach provides a first-order estimate of model sensitivity and allows the dominant parameters to be identified transparently. In addition, it allows for an assessment of whether plausible uncertainty in the experimentally determined inputs is sufficient to account for the discrepancy between the measured and predicted modulus.

The results showed that the prediction was most sensitive to fiber orientation factor, fiber modulus, and the effective length efficiency factor $\overline{\eta_l}$, followed by fiber volume content and matrix modulus. The ±5% variation was not intended as a formal uncertainty quantification, but as a simple local sensitivity test using a common perturbation magnitude for a comparative ranking of parameter influence. The predicted modulus changed by at most 3.89% for the length efficiency factor and by at least 1.11% for polymer modulus. Thus, even the most influential individual input parameter did not account for the full discrepancy between the measured and classically predicted modulus. The relative influence of the individual parameters is summarized in Figure 7.

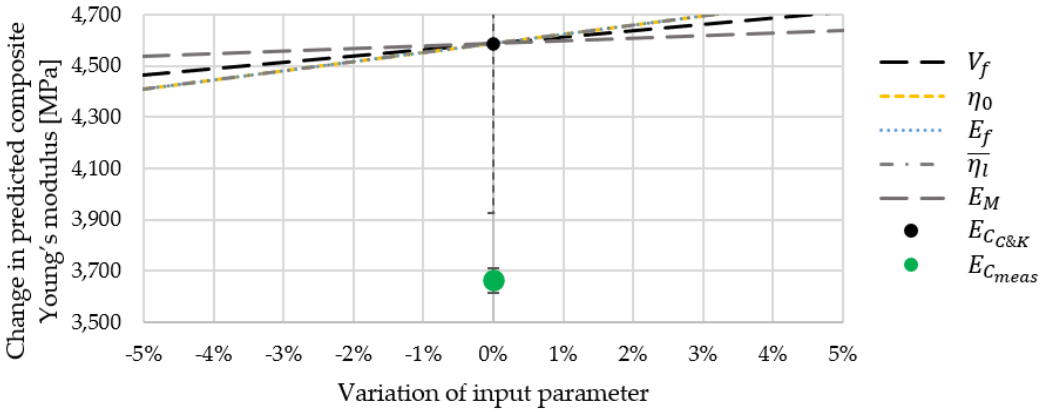

Figure 7. Sensitivity of the classical Cox–Krenchel prediction to variation of individual input parameters for a representative PP–BF composite condition. The dashed ranges represent a ±5% variation of each input parameter and show the corresponding predicted composite Young's modulus. The horizontal reference line indicates the experimentally measured Young's modulus of the selected condition. E_f, $\overline{\eta_l}$, and η_o showed identical dependencies; thus, the corresponding lines overlap.

Importantly, the analysis indicated that realistic variation of the classical input parameters alone was not sufficient to explain the systematic overestimation observed for the PP-based systems. In the representative case considered here, the minimum predicted modulus obtained within the estimated uncertainty range of one parameter was 4408 MPa, which remained about 17% above the measured value. Even when all input parameters were shifted simultaneously in the direction of lower predicted stiffness, the predicted modulus remained 3926 MPa, and thus exceeded the experimental value by 7.7%. The deviations are therefore not plausibly explained by measurement scatter alone. Instead,

the results indicate that at least one additional systematic influence is not captured by the classical formulation and are consistent with an interface-related contribution.

For the adhesion-extended model, the additional interface-related term modified the prediction only moderately because the calculated adhesion efficiency factors remained within a relatively narrow range. Nevertheless, its inclusion systematically reduced the material-dependent bias of the classical model, especially for the PP-based systems. Overall, the sensitivity analysis confirms that morphology remains the dominant basis of stiffness prediction, while the remaining systematic deviation is consistent with an additional interface-related contribution.

4.6. Improvement by the Adhesion-Extended Model

To account for interfacial effects that are not captured by fiber content, fiber length, and fiber orientation alone, the Cox–Krenchel model was extended by the adhesion efficiency factor introduced in Section 3. This factor was derived from the interfacial tension between the fiber and matrix and incorporated as an additional multiplicative term acting on the fiber-related stiffness contribution. The γ_{12} values listed in Table 7 were used directly to calculate the adhesion efficiency factors in Table 8, the corresponding modulus predictions in Table 9. The lowest adhesion efficiency factors were obtained for the PP-based systems, whereas the PA-based system exhibited the highest value, in agreement with the surface-tension analysis. Accordingly, within the present dataset, the adhesion-related correction was strongest for those composites that also showed the largest overestimation by the classical Cox–Krenchel model.

Table 8. Adhesion efficiency factors used in the adhesion-extended Cox–Krenchel model.

Material System	OWRK-Based Adhesion Efficiency Factor, η_a [-]	OWRK-Based Propagated SD [-]	WU-Based Adhesion Efficiency Factor, η_a [-]
PP–BF	0.775	0.038	0.631
PP–GF	0.786	0.027	0.645
PA–BF	0.887	0.020	0.793

Table 9. Measured mean Young's moduli and corresponding relative prediction errors of the classical and adhesion-extended Cox–Krenchel models.

Material System	Measured Mean Modulus [MPa]	Classical Prediction [MPa]	Classical Deviation [%]	Adhesion-Extended Prediction [MPa]	Extended Deviation [%]
PP–BF (2.5 vol.%)	2130	2379	+11.7	2085	−2.1
PP–BF (7.5 vol.%)	3598	4345	+20.8	3596	−0.1
PP–GF (8.5 vol.%)	3493	4223	+20.9	3533	+1.1
PA–BF (7.5 vol.%)	4862	4869	+0.1	4788	−3.1

Because the adhesion efficiency factor depends only on the matrix–fiber combination through γ_{12}, the same η_a value was used for both PP–BF systems despite their different fiber volume fractions.

The standard deviations of the calculated interfacial tensions were additionally propagated through Equation (10) to estimate the uncertainty of the adhesion efficiency factor. The resulting propagated standard deviations of η_a are included in Table 8. Because the differences in γ_{12} were moderate relative to their uncertainty, the resulting η_a values should

be interpreted primarily as trend-level descriptors of relative interfacial compatibility rather than as sharply separated deterministic quantities.

The inclusion of this additional factor reduced the predicted Young's moduli of all investigated composites relative to the classical Cox–Krenchel predictions. As a result, the agreement between the prediction and experiment improved substantially, particularly for the PP-based compounds.

For descriptive comparison, Table 9 summarizes the measured and predicted system-level mean Young's moduli. Calibration of ω and all global error metrics, however, was performed on the full set of 55 condition-specific data points.

As shown in Table 9, the improvement was most pronounced for the PP-based systems, for which the classical Cox–Krenchel model had produced the largest overestimations. For PP–BF at 7.5 vol.% and for PP–GF, the deviation was reduced from about 20–21% to values close to zero or only a few percent. In contrast, only a minor correction was required for PA–BF, where the classical prediction was already in close agreement with the experiment. For PP–BF at 2.5 vol.%, the extended model also improved agreement, although the absolute correction remained comparatively small. In the cases where the adhesion-extended model yielded a slight underprediction, the deviation remained modest relative to the previous overestimation of the classical model.

For additional reference, a one-parameter constant-factor null model was also evaluated, in which the fiber-related stiffness contribution of the classical Cox–Krenchel model was scaled by a global reduction factor c independent of the interfacial-tension data:

$$E_c = E_m\left(1 - V_f\right) + c\left(\eta_o \overline{\eta_l} E_f V_f\right) \tag{13}$$

Thus, both the adhesion-extended model and the null model introduce one fitted parameter and can be compared directly on the same data basis.

To assess robustness with respect to material-system transferability, a grouped leave-one-material-system-out cross-validation was performed for both one-parameter model extensions on the same condition-specific dataset. In each fold, one complete material system was excluded from calibration, the corresponding parameter (ω or c) was fitted on the remaining systems, and the held-out system was then predicted on condition level. Because this validation removes entire material-system groups from the training data, it provides a stricter robustness test than pointwise resampling. The corresponding results are summarized in Table 10.

Table 10. Grouped leave-one-material-system-out cross-validation (grouped LOOCV) of the adhesion-extended and constant-factor null models based on the full condition-specific dataset. In each fold, one material system was excluded from calibration and predicted on condition level.

				Adhesion-Extended Cox–Krenchel Model			Constant Factor Null Model		
Held-Out System	**Systems Used for Calibration [vol.%]**	**Measured Modulus [GPa]**	**Number of Data Points**	**Fitted ω**	**Predicted Modulus [GPa]**	**Held-Out Relative Error [%]**	**Fitted c**	**Predicted Modulus [GPa]**	**Held-Out Relative Error [%]**
PP–BF (2.5 vol.%)	PP–BF (7.5), PP–GF (8.5), PA–BF (7.5)	2.130	44	0.80	2.081	−2.3	0.78	2.093	−1.7
PP–BF (7.5 vol.%)	PP–BF (2.5), PP–GF (8.5), PA–BF (7.5)	3.598	33	0.80	3.585	−0.4	0.78	3.622	0.7
PP–GF (8.5 vol.%)	PP–BF (2.5), PP–BF (7.5), PA–BF (7.5)	3.493	39	0.73	3.581	2.5	0.79	3.551	1.6
PA–BF (7.5 vol.%)	PP–BF (2.5), PP–BF (7.5), PP–GF (8.5)	4.862	49	0.80	4.711	−3.1	0.78	4.568	−6.0

Because the cross-validation was carried out by excluding complete material-system groups rather than individual data points, the fold-specific values of ω and c reported in Table 10 are not expected to be identical to the globally calibrated parameter. Instead, they indicate how sensitively the fitted correction depends on the inclusion of a given material system and how well the model transfers to previously unseen material-system classes on condition level. Given the limited number of distinct material systems, this grouped cross-validation should be regarded as a robustness check rather than as full external validation.

Table 10 shows that both one-parameter extensions were reasonably stable under grouped cross-validation. In most folds, the adhesion-extended model and the constant-factor null model gave similarly good predictions, whereas for the PA–BF hold-out case, the adhesion-extended model performed more accurately.

The corresponding improvement in predictive accuracy is also visualized in Figure 8, which compares the measured Young's moduli with the predictions of the classical and adhesion-extended Cox–Krenchel models.

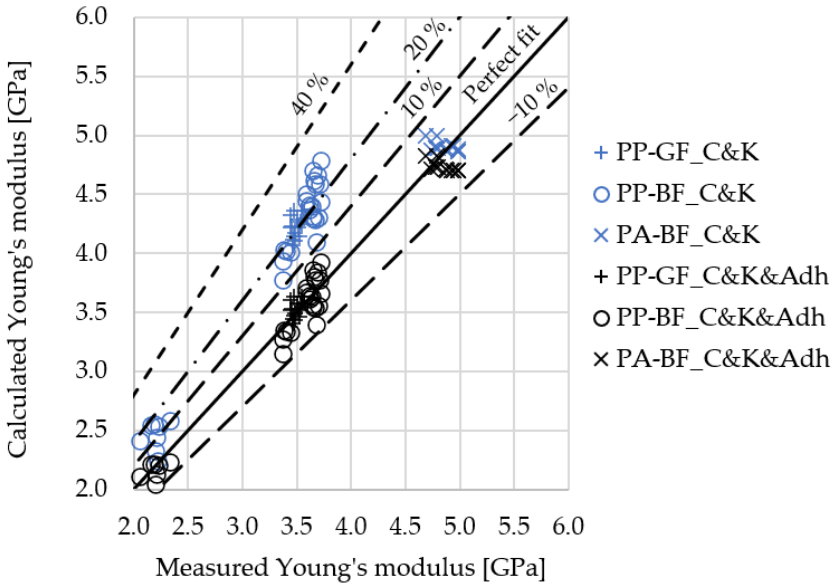

Figure 8. Comparison of measured Young's moduli with predictions of the classical (C&K) and adhesion-extended (C&K&Adh) Cox–Krenchel models.

In Figure 8, the predictions of the classical Cox–Krenchel model lay systematically above the ideal parity line for the PP-based systems, whereas the adhesion-extended predictions shifted closer to the diagonal; only minor changes were observed for PA–BF. This behavior indicates that the proposed interfacial correction not only reduces the average error, but also improves the consistency of prediction across different material systems.

This overall improvement is also reflected in the global error metrics summarized in Table 11.

Table 11. Global prediction errors of the classical, constant-factor null, and adhesion-extended Cox–Krenchel models.

Model Formulation	MAE [MPa]	RMSE [MPa]	MAPE [%]	Maximum Relative Deviation [%]
Classical Cox–Krenchel model	573.8	640.6	14.16	28.92
Constant-factor null model	106.5	146.9	3.05	10.47
Adhesion-extended Cox–Krenchel model	94.0	121.2	2.74	10.96

Compared with the classical formulation, both one-parameter extensions substantially reduced MAE, RMSE, MAPE, and the maximum relative deviation on the full dataset of 55 condition-specific data points. The adhesion-extended model yielded the lowest MAE, RMSE, and MAPE overall, while the constant-factor null model showed a slightly lower maximum relative deviation. The comparison therefore indicates that part of the residual error of the classical Cox–Krenchel model can already be reduced by a simple global scaling of the fiber contribution, but that the interfacial-tension-based formulation provides the better overall description on the present dataset. At the same time, because both extensions were calibrated on the same dataset and only a limited number of material systems is available, this advantage should be interpreted as promising rather than definitive. Broader validation across additional matrix–fiber combinations will be required to determine whether the physically motivated adhesion-based formulation provides a robust predictive advantage beyond a purely empirical global reduction factor.

4.7. Exploratory Comparison with Independent Literature Data

To examine whether the proposed adhesion-based extension is at least qualitatively transferable beyond the present in-house dataset, an additional exploratory comparison was carried out using independent literature data reported by Liu [43] for PA 6 composites reinforced with basalt fibers of different surface states. This literature-based comparison was kept separate from the calibration and condition-level validation performed on the in-house dataset and is intended as a limited plausibility check rather than as a formal external validation. The case was selected because it provides not only composite Young's modulus values, but also the constituent, morphology, and surface-tension data required for application of the classical and adhesion-extended Cox–Krenchel formulations.

The dispersive and polar surface-tension components reported by Liu [43] for the basalt-fiber surface states were combined with the literature surface-tension values for PA 6 from Milani [44] to calculate the corresponding interfacial tensions and adhesion efficiency factors according to Equations (7) and (10). The resulting interface descriptors are summarized in Table 12. Among the surface states reported by Liu [43], complete modulus-related input data for the present comparison were available for the H_2O-desized fibers and for the H_2O-desized + APS/EP-treated fibers.

Table 12. Surface-tension components and calculated interface descriptors for the independent literature comparison based on Liu [43] (*) and Milani [44] (**).

Fiber Surface State *	γ_1^d * (BF) [mN m^{-1}]	γ_1^p * (BF) [mN m^{-1}]	γ_2^d ** (PA 6) [mN m^{-1}]	γ_2^p ** (PA 6) [mN m^{-1}]	γ_{12} [mN m^{-1}]	η_a [-]
H_2O-desized basalt fiber	25.1	9.1	34.4	5.2	1.275	0.975
H_2O-desized + APS/EP-treated basalt fiber	23.9	8.5	34.4	5.2	1.361	0.973

Using the constituent and morphology parameters reported by Liu [43], namely fiber volume fraction, characteristic fiber length, orientation factor, fiber radius, and constituent moduli, the composite Young's modulus was then calculated with both the classical and adhesion-extended Cox–Krenchel formulations. The corresponding predictions and prediction deviations from the literature-reported modulus values are listed in Table 13.

As shown in Table 13, both literature cases exhibited very low calculated interfacial tensions and correspondingly high adhesion efficiency factors close to unity. This is consistent with the expectation that PA-based systems with comparatively favorable thermodynamic compatibility require only a small interface-related correction. Accordingly, the adhesion-extended model changed the classical prediction only moderately.

Table 13. Classical and adhesion-extended modulus predictions for the independent literature cases from Liu [43].

Literature Case from Liu	V_f [vol.%]	l_f [µm]	η_o [-]	r [µm]	E_f [MPa]	E_m [MPa]	Reported Modulus [MPa]	Classical Prediction [MPa]	Adhesion-Extended Prediction [MPa]	Classical Deviation [%]	Extended Deviation [%]
H_2O-desized BF/PA 6	13.24	292.2	0.91	9.65	65,000	2100	8350	9564	9370	14.5	12.2
H_2O-desized + APS/EP BF/PA 6	11.73	300.3	0.88	9.60	65,000	2100	7950	8483	8306	6.7	4.5

For the H_2O-desized basalt-fiber case, the classical Cox–Krenchel model overpredicted the reported modulus by 14.5%, whereas inclusion of the adhesion efficiency factor reduced the relative prediction error to 12.2%. For the H_2O-desized + APS/EP-treated fibers, the relative prediction error was reduced from 6.7% to 4.5%. Thus, the adhesion-based correction improved agreement in both literature cases, although the improvement remained comparatively small because the calculated η_a values were already close to one.

At the same time, the two literature cases showed only a small difference in calculated interfacial tension and adhesion efficiency factor, with

$$\eta_a = 0.975$$

for the H_2O-desized fibers and

$$\eta_a = 0.973$$

for the H_2O-desized + APS/EP-treated fibers. This is consistent with the comparatively small difference in the reported composite modulus between the two variants. In this sense, the external comparison reproduces the direction and magnitude of only a modest interface-related effect rather than a strong separation between surface states.

Overall, this independent literature comparison does not replace broader external validation across a larger and more diverse dataset. Nevertheless, it supports the plausibility of the proposed interface-related model extension in an external PA 6/basalt-fiber case and indicates that the surface-energy-based correction can be transferred consistently to independently reported composite systems when compatible constituent and morphology data are available.

5. Discussion

The present results show that the Young's modulus of short-fiber-reinforced thermoplastics cannot always be described sufficiently by constituent stiffness, fiber volume fraction, fiber length, and fiber orientation alone. Although these morphology-related quantities remain the primary determinants of stiffness and were determined experimentally in the present study, the predictive quality of the classical Cox–Krenchel model still varied systematically between material systems. In particular, the model described the PA–BF system with high accuracy, whereas it overpredicted the stiffness of the PP-based systems. Because the mechanical tests showed low scatter, the morphology input parameters were measured rather than assumed, and no pronounced fiber agglomeration or fiber-free regions were observed, the remaining deviation is most plausibly interpreted as a systematic model limitation rather than random experimental variability.

Within the classical Cox–Krenchel framework, the reinforcement efficiency of the fibers is reduced by two established mechanisms, namely finite fiber length and non-ideal orientation. Both effects were accounted for here using experimentally derived descriptors. Nevertheless, the sensitivity analysis showed that realistic variation of these classical input parameters was not sufficient to explain the systematic overestimation observed for the PP-based compounds. This supports the conclusion that an additional system-dependent factor influences the effective elastic stress transfer. The surface-tension analysis provides a plausible basis for such an interpretation, because the PP-based systems exhibited higher interfacial tension than the PA-based system and therefore less favorable thermodynamic compatibility within the present descriptor framework.

The incorporation of the adhesion efficiency factor improved agreement between the predicted and measured Young's moduli, particularly for the PP-based materials. This is conceptually important because the proposed correction does not replace the classical micromechanical description but complements it. Fiber volume fraction, the effective Cox length efficiency factor derived from the measured fiber lengths, and fiber orientation remain the dominant structural descriptors, whereas the adhesion-related term acts as a secondary correction for system-dependent differences in effective load-transfer quality. In this sense, the present approach should be understood as an interface-sensitive refinement of the Cox–Krenchel model rather than as an alternative to morphology-based micromechanics.

Application of the harmonic-mean rule according to Wu yielded substantially higher absolute interfacial-tension values than the OWRK relation for all investigated systems, and consequently lower adhesion efficiency factors when the same value of ω was inserted. However, the ranking of the investigated fiber–polymer combinations was preserved. This indicates that the proposed interface-related descriptor is qualitatively robust with respect to the combining rule, although the absolute scale of γ_{12} and η_a is rule-dependent. Accordingly, ω is not a universal material constant but a calibration parameter linked to the selected interfacial-tension formalism. To obtain adhesion efficiencies of comparable magnitude, the proportionality constant ω would have to be reduced from 0.8 to approximately 0.43, further confirming that ω is not a universal material constant but depends on the selected interfacial-tension formalism.

At the same time, the interpretation of the adhesion factor requires caution. The quantity used here is derived from surface-tension-based interfacial tension and is therefore a thermodynamic descriptor of compatibility rather than a direct mechanical measure of interfacial strength. The model does not imply that interfacial failure occurs during modulus determination. Instead, it assumes that less favorable interfacial compatibility can reduce the transferable elastic fiber contribution in the small-strain regime, for example, through incomplete molecular-scale contact, poorly wetted regions, interphase effects, or residual-stress-related imperfections. The proposed adhesion efficiency factor should therefore be regarded as a physically motivated effective parameter rather than as a complete mechanistic description of the interface.

This restriction is also relevant because the experimentally characterized fiber surface was the as-supplied commercial fiber surface including the manufacturer-applied sizing. From the standpoint of practical composites, this is appropriate, since the matrix interacts with the sized fiber rather than with the bare mineral substrate. At the same time, the present approach does not separate substrate effects from sizing chemistry. The effective interface descriptor therefore reflects the real matrix-facing reinforcement surface of the investigated commercial systems, but matrix-dependent differences in compatibility may partly arise from the applied sizing rather than from intrinsic basalt-versus-glass or polymer-versus-fiber polarity alone.

A further point concerns the statistical separation of the interface descriptor. Although the calculated interfacial tensions followed a physically plausible ranking, the absolute differences between systems were relatively small compared with their propagated uncertainty. Accordingly, the present dataset supports the interpretation that interfacial compatibility contributes to the residual model error, but it does not yet allow for strong claims about the robust discrimination of closely spaced adhesion states. The adhesion-related correction should therefore presently be viewed as a semi-empirical but physically interpretable parameterization whose broader discriminating power remains to be demonstrated.

The structure of the dataset imposes an additional limitation on interpretation. Although two matrices and two mineral fiber types were considered, only three out of the four possible matrix–fiber combinations were investigated experimentally. In particular, the PA 6.6–GF combination was not available. As a result, matrix identity and interfacial-tension level are not fully disentangled in the present dataset: both PP-based systems showed comparatively higher interfacial tension and were overpredicted by the classical model, whereas the single PA-based system showed lower interfacial tension and was described accurately. This pattern is consistent with an interface-related explanation, but it does not yet exclude alternative matrix-specific contributions, such as differences in neat-polymer versus in-composite matrix stiffness, crystallization effects, residual thermal stresses, or moisture-related influences in PA 6.6. Inclusion of the missing PA 6.6–GF combination would therefore be especially valuable in future work.

The proposed correction must also be considered in relation to model form. The exponential adhesion factor introduced here is physically motivated by an attenuation assumption, but it is not unique. Other functional forms, including simpler linear or constant-factor corrections, can also reduce prediction error on a limited dataset. Indeed, the present comparison with a one-parameter constant-factor null model shows that part of the improvement may be attributable to the introduction of an additional calibratable degree of freedom itself. The relevance of the present formulation therefore lies less in claiming universal superiority at this stage than in providing a correction term with an independent physical interpretation linked to measurable interfacial properties.

The range of applicability of the present model is further limited by the scope of the investigated materials. The study focused on comparatively low to moderate fiber volume fractions and on Young's modulus under small-strain elastic loading. The proposed formulation was not developed for strength, failure strain, impact behavior, creep, or fatigue, where interfacial effects may involve debonding, frictional sliding, crack deflection, or damage accumulation. Extension of the present adhesion-related concept to strength-oriented micromechanical models, for example, Kelly–Tyson-type approaches for unidirectional composites, would therefore be an interesting subject for future work. Likewise, the present dataset covers only a modest range of interfacial-tension values, so the resulting adhesion efficiency factors varied within a comparatively narrow interval. Broader validation across higher reinforcement contents, additional polymer classes, different sizing systems, coupling-agent-modified interfaces, and wider interfacial-compatibility ranges will be necessary to assess the generality of the concept.

Another simplification concerns the thermodynamic basis of the interface descriptor itself. The interfacial tensions were calculated from surface-tension components determined at or referenced to standard conditions, whereas actual wetting and interface formation during compounding and injection molding occur in the molten state and depend on temperature, viscosity, pressure, and processing history. The present approach therefore does not resolve the full thermo-rheological complexity of interface formation. Rather, it assumes that room-temperature or literature-based surface-energy relations provide a sufficiently meaningful comparative descriptor of the resulting interface state. This

approximation appears useful within the present systems, but it should be interpreted as a simplifying engineering assumption rather than a full process-resolved interface model.

Despite these limitations, the present approach has practical advantages. Surface-energy characterization is experimentally less demanding than many direct interface tests, and the proposed correction can be incorporated into an established analytical model without sacrificing transparency. Direct mechanical methods such as pull-out, fragmentation, or microbond testing remain highly valuable for targeted interface characterization, but they often require dedicated specimen concepts and are not always readily transferable across different material systems or processing states. In this context, the use of an interfacial-tension-based descriptor may offer a pragmatic route for comparative material screening and for first-order interface-sensitive stiffness assessment when only constituent and morphology data are available.

The additional exploratory comparison with independent literature data supports this interpretation, although only in a limited sense. The literature-based cases were not part of model calibration and therefore provide a useful plausibility check beyond the in-house dataset. However, they do not substitute for broader external validation, especially because the number of distinct material systems remains small. The grouped leave-one-material-system-out cross-validation likewise provides only an initial robustness check rather than definitive evidence of general transferability.

Taken together, the present findings suggest that interfacial compatibility does not replace morphology as the dominant basis of stiffness prediction, but it can provide a meaningful second-order descriptor for residual system-dependent error. The main contribution of this work is therefore not the proposal of a fully general interface law, but the demonstration that a physically interpretable, surface-energy-based correction can improve an established Cox–Krenchel-type description of short-fiber-reinforced thermoplastics. Future work should examine broader material combinations, include the missing PA 6.6–GF system, test alternative forms of the adhesion factor, relate surface-energy-based predictions more directly to independent mechanical interface measurements, and evaluate the transferability of the present concept to thermosetting matrix systems such as epoxy or unsaturated polyester reinforced with glass or carbon fibers.

6. Conclusions

This study examined whether the remaining prediction deviation between experimentally measured Young's moduli and classical Cox–Krenchel predictions for short-fiber-reinforced thermoplastics can be reduced by including a surface-energy-based descriptor of fiber–polymer interfacial compatibility. Based on the investigated PP- and PA-based systems reinforced with basalt and glass fibers, the following conclusions can be drawn:

1. The classical Cox–Krenchel model captured the general reinforcing effect of short fibers, but its predictive accuracy depended strongly on the matrix–fiber combination and systematically overpredicted the PP-based systems.
2. Experimentally determined fiber volume fraction, the effective Cox length efficiency factor derived from measured fiber lengths, and fiber orientation remained the dominant descriptors of stiffness and provided the essential basis for micromechanical prediction.
3. Introducing an adhesion efficiency factor derived from interfacial tension improved agreement between the predicted and measured Young's moduli within the present dataset while preserving the analytical structure and simplicity of the Cox–Krenchel framework.

4. The improvement was strongest for the systems with less favorable surface-energy-based compatibility, whereas only minor corrections were required where the classical model already performed well.
5. The proposed interface-related correction should presently be regarded as a physically motivated effective parameter rather than as a complete mechanistic description of interfacial load transfer, and broader validation across additional material systems is still required.

Overall, the results indicate that morphology remains the primary basis of stiffness prediction, while surface-energy-based interfacial compatibility can serve as a useful second-order descriptor for reducing residual system-dependent error. The proposed extension therefore offers a simple and practically accessible route toward the interface-sensitive refinement of classical stiffness prediction for short-fiber-reinforced thermoplastics.

Supplementary Materials: The following supporting information can be downloaded at https://www.mdpi.com/article/10.3390/fib14090107/s1, Table S1: Investigated processing conditions; Table S2: Condition-specific experimental and model-evaluation values.

Funding: This work was supported by the German Federal Ministry for Economic Affairs and Energy under grant number KF2184742EB4.

Data Availability Statement: The raw data supporting the conclusions of this article will be made available by the author on request.

Acknowledgments: The author gratefully acknowledges funding from the "Thüringer Ministerium für Wirtschaft, Landwirtschaft und ländlichen Raum" and the "Bundesministerium für Wirtschaft und Energie" (KF2184742EB4). The author further acknowledges the Thuringian Center of Innovation in Mobility (ThIMo, current funding phase 2023 IZN 0005), Technische Universität Ilmenau, and the Thuringian Center of Mechanical Engineering (ThZM, current funding phase 2023 IZN 0004) for supporting this research by providing the necessary research infrastructure.

Conflicts of Interest: The author declares no conflicts of interest.

Abbreviations

The following abbreviations are used in this manuscript:

PP	Polypropylene
PA	Polyamide
PA 6.6	Polyamide 6.6
OWRK	Owens–Wendt–Rabel–Kaelble
BF	Basalt fiber
GF	Glass fiber
SD	Standard deviation
grouped LOOCV	Grouped leave-one-material-system-out cross-validation

References

1. Aurich, T. Spritzgießen und Resultierende Verbundeigenschaften von Flachsfaserverstärktem Polypropylen. Ph.D. Thesis, Technische Universität Chemnitz, Chemnitz, Germany, July 2000.
2. Rüschendorf, S.; Kriwet, A.; Urban, F.; Schröder, K.U. Application of artificial neural networks for predicting viscoelastic properties of short-fiber reinforced thermoplastics. *Comput. Mater. Sci.* **2026**, *262*, 114409. [CrossRef]
3. Lafranche, É.; Martins, C.I.; Oliveira, V.M.; Krawczak, P. Prediction of tensile properties of injection moulding flax fibre reinforced polypropylene from morphology analysis. *Key Eng. Mater.* **2013**, *554–557*, 1573–1582. [CrossRef]
4. Potluri, R.; Diwakar, V.; Venkatesh, K.; Srinivasa Reddy, B. Analytical Model Application for Prediction of Mechanical Properties of Natural Fiber Reinforced Composites. *Mater. Today Proc.* **2018**, *5*, 5809–5818. [CrossRef]
5. Andre, N.; Ariawan, D.; Mohd Ishak, Z. Elastic anisotropy of kenaf fibre and micromechanical modeling of nonwoven kenaf fibre/epoxy composites. *J. Reinf. Plast. Compos.* **2016**, *35*, 1424–1433. [CrossRef]

6. van den Oever, M.J.A.; Bos, H.L.; van Kemenade, M.J.J.M. Influence of the Physical Structure of Flax Fibres on the Mechanical Properties of Flax Fibre Reinforced Polypropylene Composites. *Appl. Compos. Mater.* **2000**, *7*, 387–402. [CrossRef]
7. Oumer, A.N.; Bachtiar, D. Modeling and experimental validation of tensile properties of sugar palm fiber reinforced high impact polystyrene composites. *Fibers Polym.* **2014**, *15*, 334–339. [CrossRef]
8. Yaghoobi, H.; Fereidoon, A. Modeling and optimization of tensile strength and modulus of polypropylene/kenaf fiber biocomposites using Box–Behnken response surface method. *Polym. Compos.* **2018**, *39*, E463–E479. [CrossRef]
9. Hine, P.; Parveen, B.; Brands, D.; Caton-Rose, F. Validation of the modified rule of mixtures using a combination of fibre orientation and fibre length measurements. *Compos. Part A Appl. Sci. Manuf.* **2014**, *64*, 70–78. [CrossRef]
10. Puch, F. Herstellung und Eigenschaften von Kohlenstoffnanoröhrchen-Polyamid 6-Kompositen. Ph.D. Thesis, Rheinisch-Westfälische Technische Hochschule Aachen, Aachen, Germany, 2015.
11. Rivas-Menchi, A.; Herrera-Franco, P.J.; Valadez-González, A.; Carrillo, J.G.; May-Pat, A. A novel approach for the practical estimation of the elastic modulus in randomly oriented short fiber reinforced composites. *J. Compos. Mater.* **2025**, *59*, 2559–2571. [CrossRef]
12. Jiang, Q.; Takayama, T.; Nishioka, A. Improving the Accuracy of the Evaluation Method for the Interfacial Shear Strength of Fiber-Reinforced Thermoplastic Polymers through the Short Beam Shear Test. *Polymers* **2024**, *16*, 883. [CrossRef] [PubMed]
13. Guo, G.; Yang, Z.; Cai, M.; Wang, S.; Jiang, L. Surface Activation and Characterization of Basalt Fiber by Plasma Treatment and Its Interfacial Adhesion with Epoxy. *Polymers* **2024**, *16*, 3181. [CrossRef] [PubMed]
14. Potente, H. *Fügen von Kunststoffen—Grundlagen, Verfahren, Anwendung*; Carl Hanser Verlag: München, Germany, 2004.
15. Haufe, M. Methoden zur Verbesserung der Adhäsion von Klebstoffen an Metallischen Oberflächen. Ph.D. Thesis, Universität Bielefeld, Bielefeld, Germany, March 2002.
16. Chen, L. Dynamic Wetting by Viscous Liquids: Effects of Softness, Wettability and Curvature of the Substrate and Influence of External Electric Fields. Ph.D. Thesis, Technische Universität Darmstadt, Darmstadt, Germany, 2013.
17. Young, T. An Essay on the Cohesion of Fluids. *Philos. Trans. R. Soc. Lond.* **1805**, *95*, 65–87. [CrossRef]
18. Njobuenwu, D.; Oboho, E.O.; Gumus, R.H. Determination of Contact Angle from Contact Area of Liquid Droplet Spreading on Solid Substrate. *Leonardo Electron. J. Pract. Technol.* **2007**, *10*, 29–38.
19. Pochly, F.; Fialová, S.; Kozubkova, M.; Zavadil, L. Study of the Adhesive Coefficient Effect on the Hydraulic Losses and Cavitation. *Int. J. Fluid Mach. Syst.* **2010**, *3*, 386–395. [CrossRef]
20. Harkins, W.D. *Physical Chemistry of Surface Films*; OCLC 1508905, LCCN 52006111; Reinhold Publishing Corp.: New York, NY, USA, 1952; 413p.
21. Raos, G.; Zappone, B. Polymer Adhesion: Seeking New Solutions for an Old Problem. *Macromolecules* **2021**, *54*, 10617–10644. [CrossRef]
22. Voiutskii, S.S. *Autohesion and Adhesion of High Polymers*; Interscience: New York, NY, USA, 1963; 272p.
23. Lee, L.H. Adhesion of High Polymers. I. Influence of Diffusion, Adsorption, and Physical State on Polymer Adhesion. *J. Polym. Sci. Part A-2 Polym. Phys.* **1967**, *5*, 751–760. [CrossRef]
24. Bischof, C.; Possart, W. *Adhäsion—Theoretische und Experimentelle Grundlagen*; Akademie-Verlag: Berlin, Germany, 1983. [CrossRef]
25. Habenicht, G. *Kleben—Grundlagen, Technologien, Anwendungen*; Springer: Berlin, Germany, 2009.
26. Eötvös, R. Ueber den Zusammenhang der Oberflächenspannung der Flüssigkeiten mit ihrem Molecularvolumen. *Ann. Phys.* **1886**, *263*, 448–459. [CrossRef]
27. Brockmann, W. Über Haftvorgänge beim Kleben. *Adhäsion* **1969**, *13*, 335–342.
28. Uba, C.U.; Raush, J.R. Quantification of Wettability and Surface Tension of Liquid Aluminum 7075 Alloy on Various Substrates. *J. Manuf. Mater. Process.* **2025**, *9*, 165. [CrossRef]
29. Owens, D.K.; Wendt, R.C. Estimation of the Surface Free Energy of Polymers. *J. Appl. Polym. Sci.* **1969**, *13*, 1741–1747. [CrossRef]
30. Kaelble, D.H. Dispersion-Polar Surface Tension Properties of Organic Solids. *J. Adhes.* **1970**, *2*, 66–81. [CrossRef]
31. Rabel, W. Einige Aspekte der Benetzungstheorie und ihre Anwendung auf die Untersuchung und Veränderung der Oberflächeneigenschaften von Polymeren. *Farbe Lack.* **1971**, *77*, 997–1005.
32. Fowkes, F.M. Attractive Forces at Interfaces. *Ind. Eng. Chem.* **1964**, *56*, 40–52. [CrossRef]
33. Owens, D.K. Some Thermodynamic Aspects of Polymer Adhesion. *J. Appl. Polym. Sci.* **1970**, *14*, 1725–1730. [CrossRef]
34. Demarquette, N.R.; Kamal, M.R. Interfacial Tension in Polymer Melts. I: An Improved Pendant Drop Apparatus. *Polym. Eng. Sci.* **1994**, *34*, 1823–1833. [CrossRef]
35. Escudie, E. Pendent drop measurements of the polypropylene/polystyrene interfacial tension between 220 °C and 270 °C. *Mater. Chem. Phys.* **1986**, *14*, 239–246. [CrossRef]
36. Roe, R.-J. Surface Tension of Polymer Liquids. *J. Phys. Chem.* **1968**, *72*, 2013–2017. [CrossRef]
37. Schultz, J.; Nardin, M. Theories and Mechanisms of Adhesion. In *Handbook of Adhesive Technology*, 2nd ed.; Pizzi, A., Mittal, K.L., Eds.; Marcel Dekker Inc.: New York, NY, USA, 2003; ISBN 0-8247-0986-1.

38. *DIN EN ISO 19403-1*; Paints and Varnishes—Wettability—Part 1: Terminology and General Principles. Beuth Verlag GmbH: Berlin, Germany, 2020.
39. Zisman, W.A. Influence of Constitution on Adhesion. *Ind. Eng. Chem.* **1963**, *55*, 18–38. [CrossRef]
40. Mäder, E.; Jacobasch, H.-J.; Grundke, K.; Uhlmann, P.; Simon, F. Comparison of surface-chemical methods for characterizing carbon fiber-epoxy resin composites. *Compos. Interfaces* **1996**, *3*, 293–320. [CrossRef]
41. Wu, S. Calculation of Interfacial Tension in Polymer Systems. *J. Polym. Sci. Part C Polym. Symp.* **1971**, *34*, 19–30. [CrossRef]
42. Crimmann, P. Grenzflächenmodifizierung und -Analyse im Polypropylen-Kupfer-Verbund. Ph.D. Thesis, Martin-Luther-Universität Halle-Wittenberg, Halle (Saale), Germany, 2003.
43. Liu, J. Untersuchung von Verbundwerkstoffen mit Basalt- und PBO-Faser-Verstärkung. Ph.D. Thesis, Technische Universität Dresden, Dresden, Germany, 2008.
44. Milani, R. Chlorinated Phosphazene Materials for Surface Functionalization, Synthesis of Monomeric Precursors and Supramolecular Chemistry. Ph.D. Thesis, University of Padova, Padova, Italy, 2008.
45. Hillström, L.; Valdek, U.; Lundberg, B. Estimation of the State Vector and Identification of the Complex Modulus of a Beam. *J. Sound Vib.* **2003**, *261*, 653–673. [CrossRef]
46. Kunz, J. Die Querkontraktionszahl in der Konstruktionspraxis. *KunststoffXtra* **2011**, *6*, 27–30.
47. *DIN EN ISO 527-2*; Plastics—Determination of Tensile Properties—Part 2: Test Conditions for Moulding and Extrusion Plastics. Beuth Verlag GmbH: Berlin, Germany, 2012.
48. *DIN EN ISO 527-1*; Plastics—Determination of Tensile Properties—Part 1: General Principles. Beuth Verlag GmbH: Berlin, Germany, 2012.
49. *DIN EN ISO 1172*; Textile-Glass-Reinforced Plastics—Prepregs, Moulding Compounds and Laminates—Determination of the Textile-Glass and Mineral-Filler Content—Calcination Methods. Beuth Verlag GmbH: Berlin, Germany, 2023.
50. Gigante, V.; Cartoni, F.; Dal Pont, B.; Aliotta, L. Extrusion Parameters Optimization and Mechanical Properties of Bio-Polyamide 11-Based Biocomposites Reinforced with Short Basalt Fibers. *Polymers* **2024**, *16*, 3092. [CrossRef] [PubMed]
51. Mohajerani, A.; Hui, S.-Q.; Mirzababaei, M.; Arulrajah, A.; Horpibulsuk, S.; Abdul Kadir, A.; Rahman, M.T.; Maghool, F. Amazing Types, Properties, and Applications of Fibres in Construction Materials. *Materials* **2019**, *12*, 2513. [CrossRef] [PubMed]

Disclaimer/Publisher's Note: The statements, opinions and data contained in all publications are solely those of the individual author(s) and contributor(s) and not of MDPI and/or the editor(s). MDPI and/or the editor(s) disclaim responsibility for any injury to people or property resulting from any ideas, methods, instructions or products referred to in the content.